星・惑星系の形成過程 入門

中本泰史 (東工大)

1. 形成過程の概観
2. 分子雲の重力収縮
3. 原始惑星系円盤
4. 固体微粒子の進化
5. 微惑星から惑星へ
6. 惑星系の形成

原始惑星系円盤内での進化

0.1μmから10000kmへ

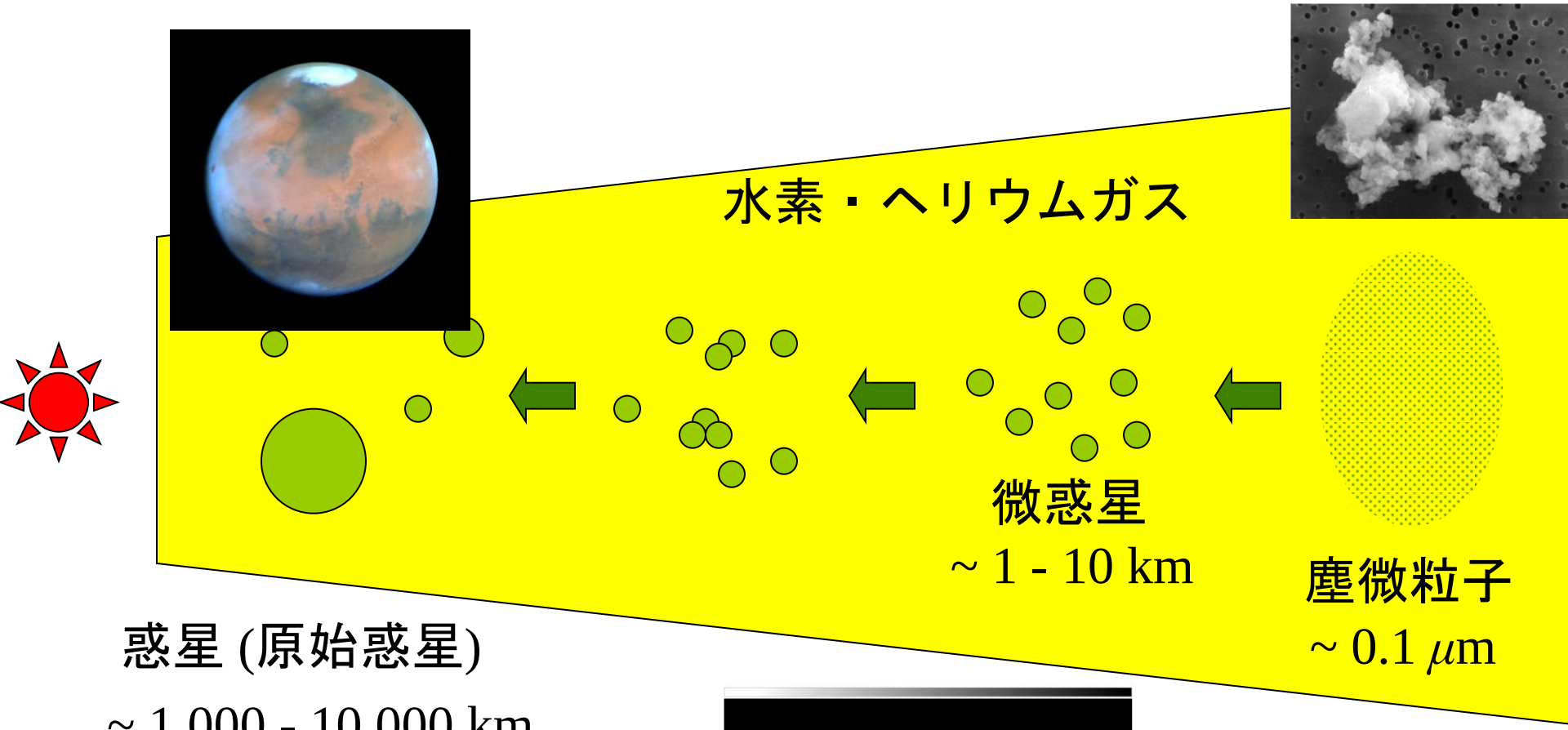

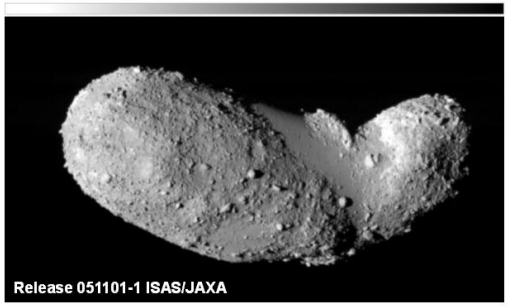

図3 イトカワの +90 度面

ダストの結晶化

大規模移動？

星形成領域

オリオン座分子雲

固体微粒子

組成：
- 氷
- 岩石質

大きさ：
- 0.1μm程度以下

結晶性：
- 非晶質
  (ガラス，アモルファス)

結晶 (水晶)

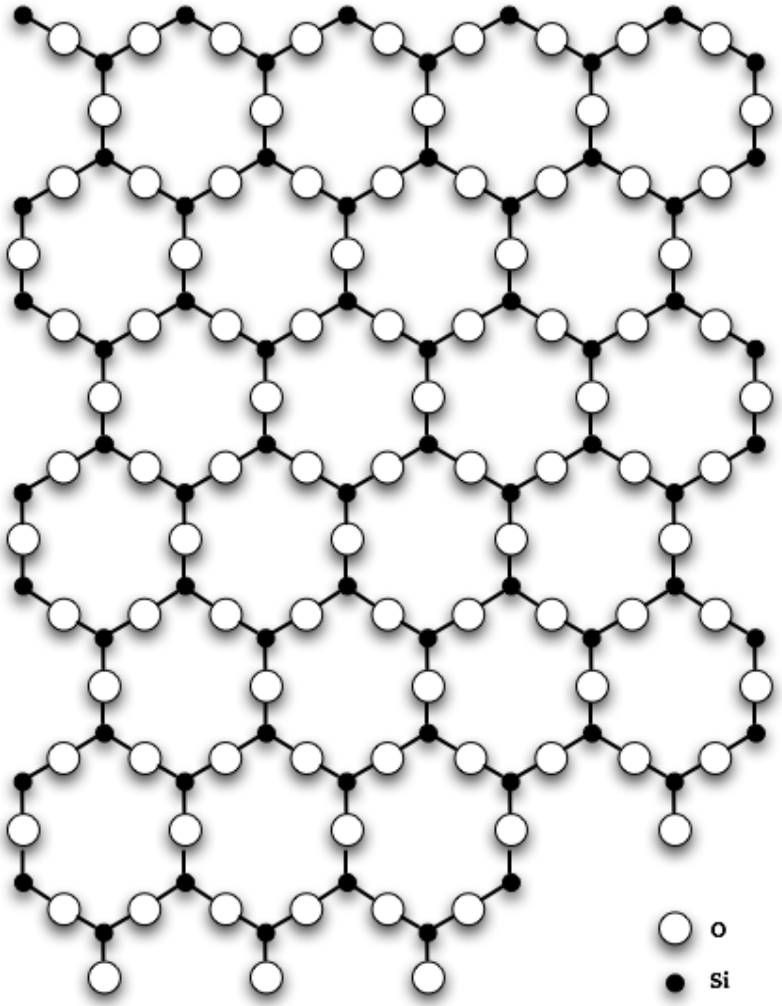

非晶質 (石英ガラス)

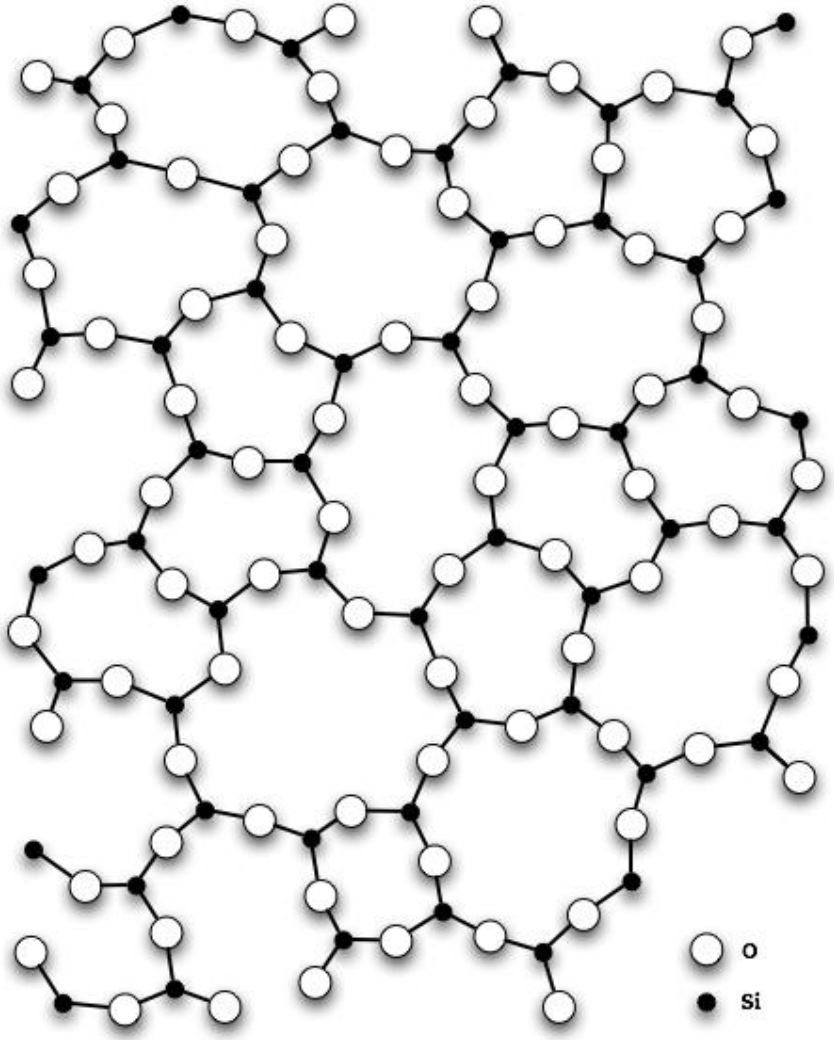

原始惑星系円盤

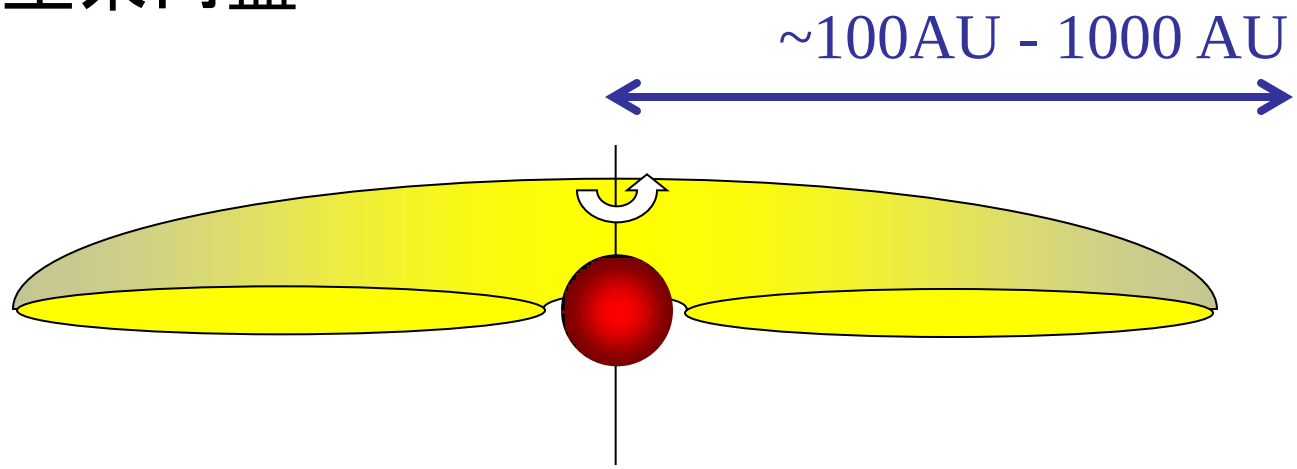

円盤質量： ~0.001 – 0.1 太陽質量

質量比
ガス(水素・ヘリウム)： 99%
固体微粒子　　： 1%

van Boekel et al. 2004

Table 1 **Dust properties in the inner and outer disk**

	Crystallinity (%)		Fraction of large grains (%)		Crystalline olivine to pyroxene ratio	
	Inner disk	Outer disk	Inner disk	Outer disk	Inner disk	Outer disk
HD 163296	40^{+20}_{-20}	15^{+10}_{-10}	95^{+5}_{-10}	65^{+20}_{-20}	$2.3^{+3.7}_{-0.5}$	–
HD 144432	55^{+30}_{-20}	10^{+10}_{-5}	90^{+10}_{-10}	35^{+20}_{-20}	$2.0^{+1.8}_{-0.6}$	–
HD 142527	95^{+5}_{-15}	40^{+20}_{-15}	65^{+15}_{-10}	80^{+10}_{-30}	$2.1^{+1.3}_{-0.7}$	$0.9^{+0.2}_{-0.1}$

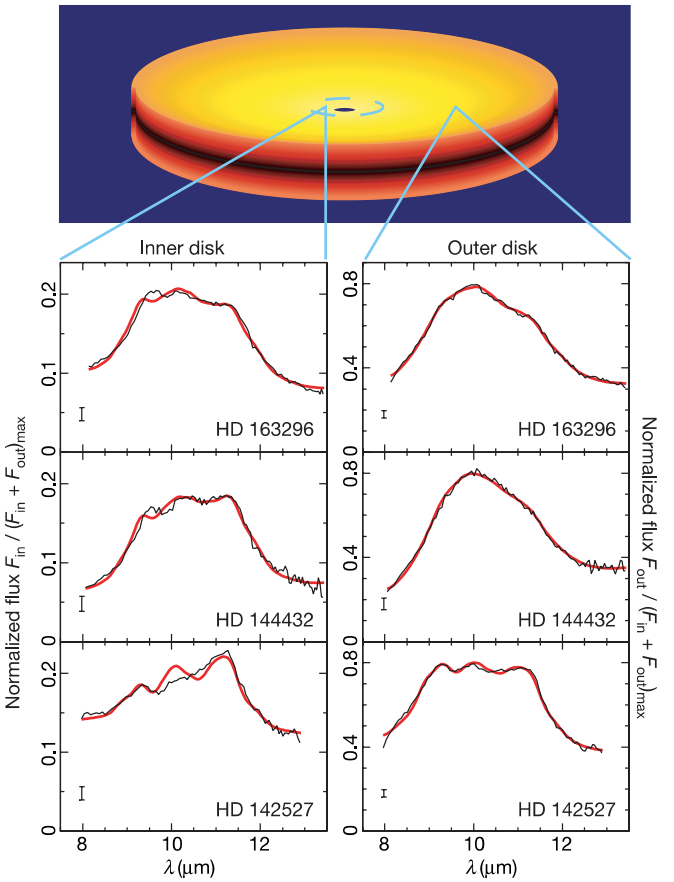

Figure 2 Infrared spectra of the inner (1–2 AU) and outer (2–20 AU) disk regions of three Herbig Ae stars. The outer-disk spectrum of each source has been constructed by subtracting the correlated spectrum from the total-disk spectrum (see ref. 8). The regions that dominate the inner- and outer-disk spectra are indicated in the schematic representation of a proto-planetary disk at the top of the figure (not to scale). The flux levels are scaled such that the sum of the inner- and outer-disk spectrum, that is, the total-disk spectrum, is normalized to unity. This allows the relative contributions of the inner and outer disk to the total spectrum to be estimated easily from this figure. The uncertainties in the spectra are indicated by the error bars in the lower left corner of each graph. The differences in shape between the inner- and outer-disk spectra are clearly visible in all three sources, indicating a difference in dust mineralogy. The broadening of the feature as seen in the inner-disk spectra indicates grain growth, whereas the resonance at 11.3 μm indicates the presence of crystalline silicates (see also Fig. 1). Also shown are the best-fit model spectra for the inner- and outer-disk regions (red lines, see also Table 1). The model spectra reproduce the observed spectral shapes, although the fits to the inner disk spectra are less good than the fits to the outer-disk spectra.

Herbig Ae/Be星
質量 = 太陽質量の数倍
形成期の若い星

Abraham et al. 2009

EX Lupi：M0型星, “EXors” (間欠的 outburstを起こす)

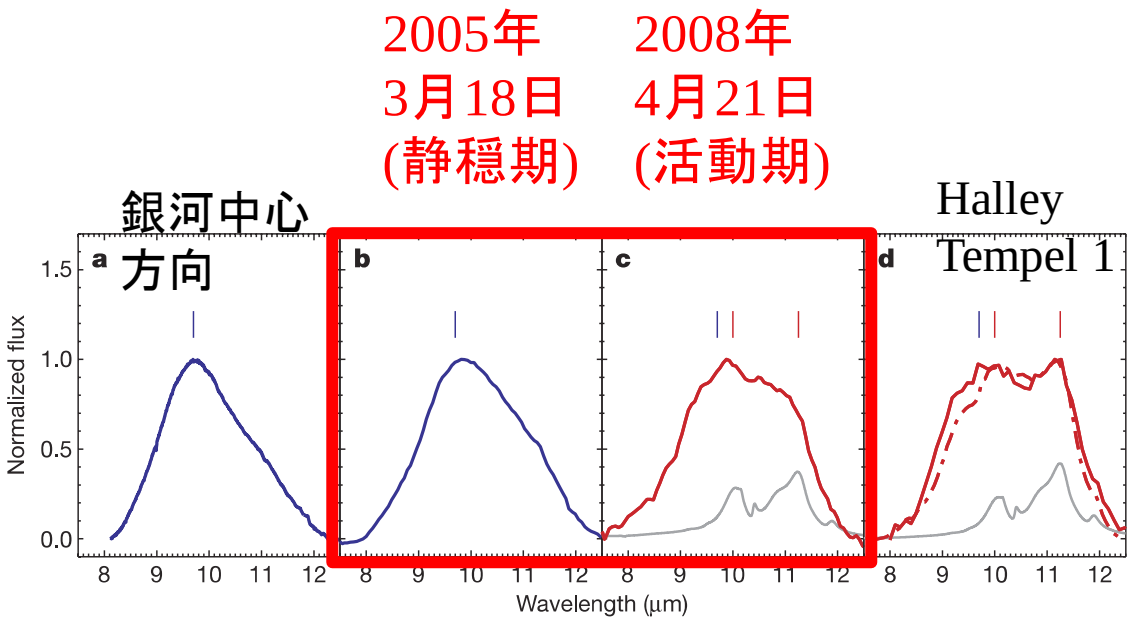

Figure 1 | Silicate emission in the 8–12-μm range. **a**, Spectrum of interstellar grains measured in the direction of the Galactic Centre[1]. **b**, Spitzer Infrared Spectrograph spectrum of EX Lupi, obtained on 2005 March 18, in quiescent phase. **c**, Our Spitzer spectrum of EX Lupi, obtained on 2008 April 21, in the middle of the present outburst. **d**, Red line, ground-based spectrum of Comet 1P/Halley[3]; dash–dot line, Spitzer spectrum of the ejecta from Comet 9P/Tempel 1 during the Deep Impact experiment[14] (available in the Spitzer archive). After a linear continuum removal, the spectra were normalized to their peak values. In **a**, we see the characteristic triangular shape profile attributed to amorphous silicate grains[1]; the vertical blue dash at 9.7 μm (repeated in all panels) corresponds to the peak wavelength of the amorphous silicate profile as measured in the laboratory[11]. In **b**, the EX Lupi spectrum closely resembles the amorphous profile, with some slight excess on the long-wavelength side. In **c**, peaks and shoulders due to crystalline silicates can be identified. Peak wavelengths of forsterite at 10.0 and 11.2 μm, as measured in laboratory experiments[12,13], are marked by red dashes. The grey curves in **c** and **d** display the emissivity curve of pure forsterite[13], assuming representative silicate grain temperatures of 1,250 K and 300 K, respectively. Panel **d** shows that the same crystalline features can be observed in cometary spectra.

Sargent et al. 2009

T Tauri型星 65個
おうし座分子雲
Spitzer望遠鏡で観測

- 結晶化ダストは
  たくさんある
- サイズ成長した
  (数ミクロン)
  ダストを持つ
  円盤は少ない

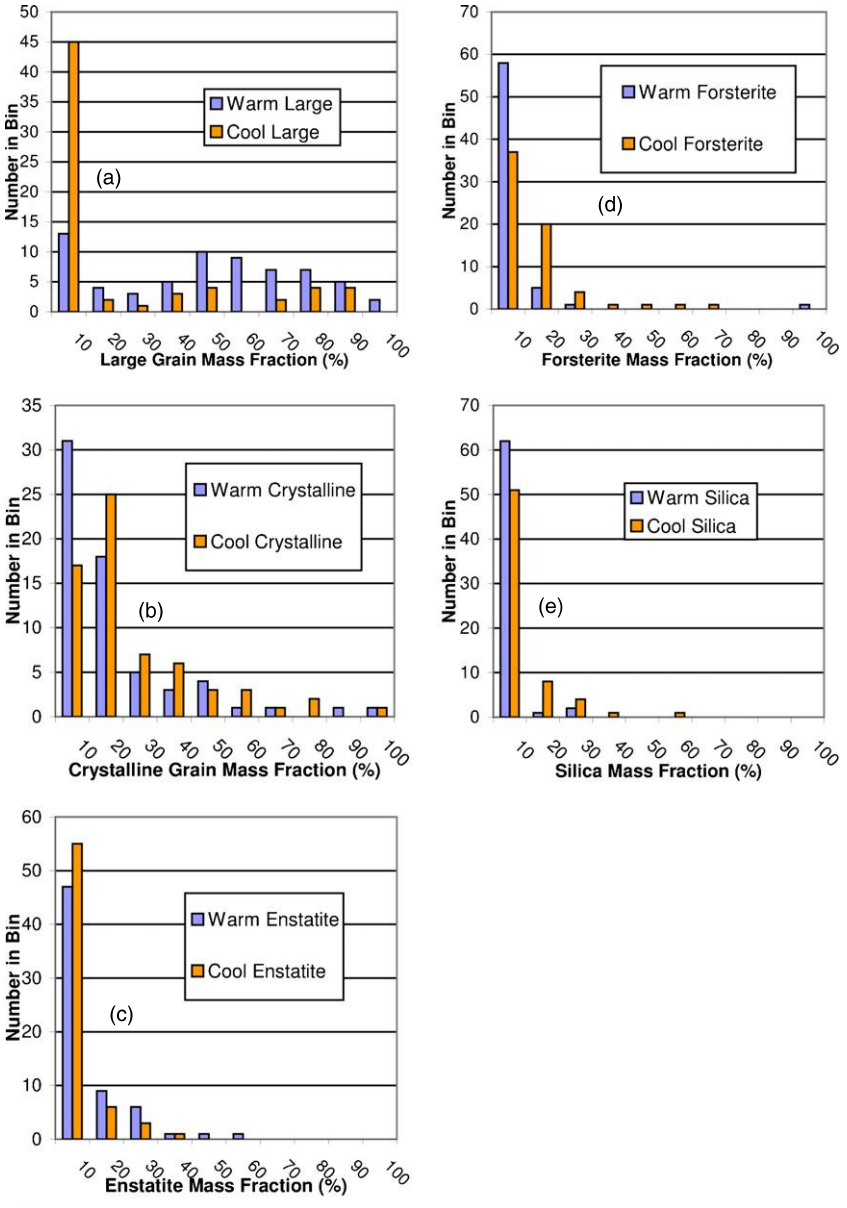

Figure 15. Warm vs. cool dust histograms. In the upper left is the large grain mass fraction histogram. In the middle left is the crystalline grain mass fraction histogram. In the lower left is the enstatite grain mass fraction histogram. In the upper right is the forsterite grain mass fraction histogram. In the lower right is the silica grain mass fraction histogram. The number of models requiring warm grain mass fractions within a given bin is represented by the height of the blue rectangle to the left within that bin. The orange rectangles to the right are for cool grain mass fractions.

Charles et al. 2011
(NASA press-release)

HOPS-68 (オリオン星雲)

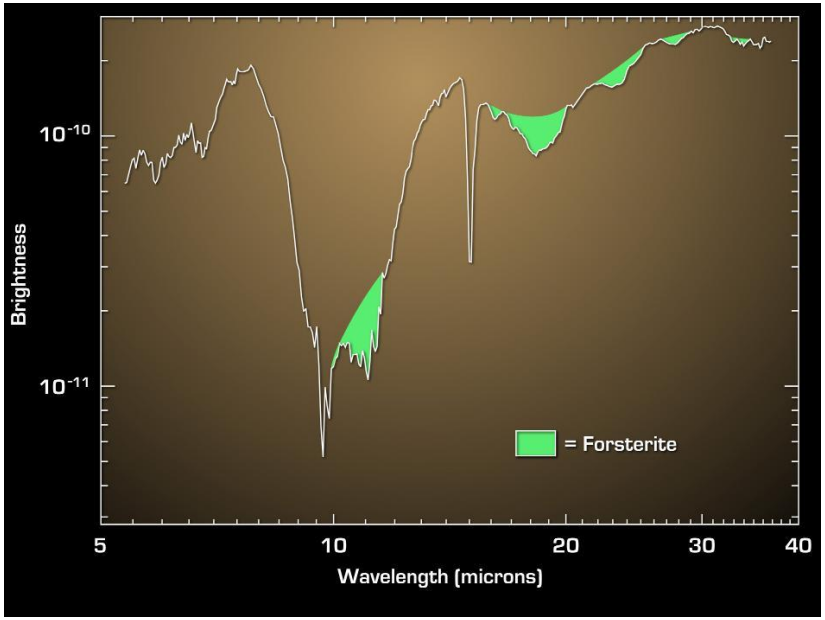

落下する雲中にダストがある
← アウトフローで巻き
　上げられたものだろう

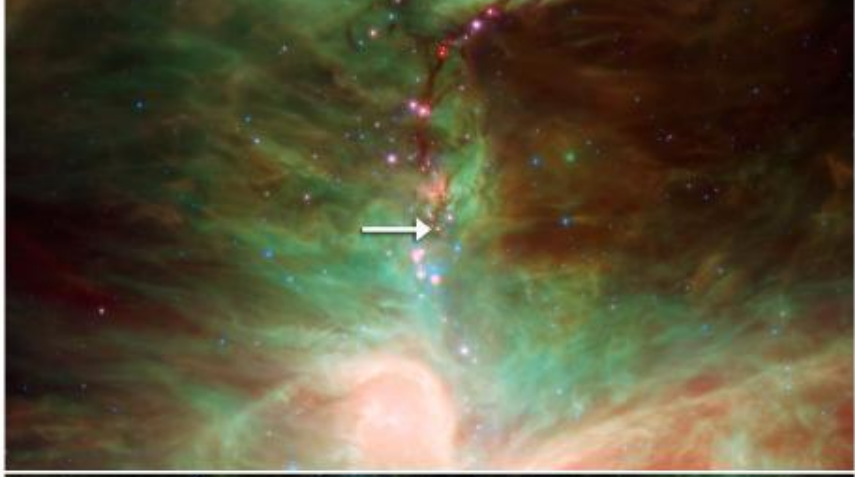

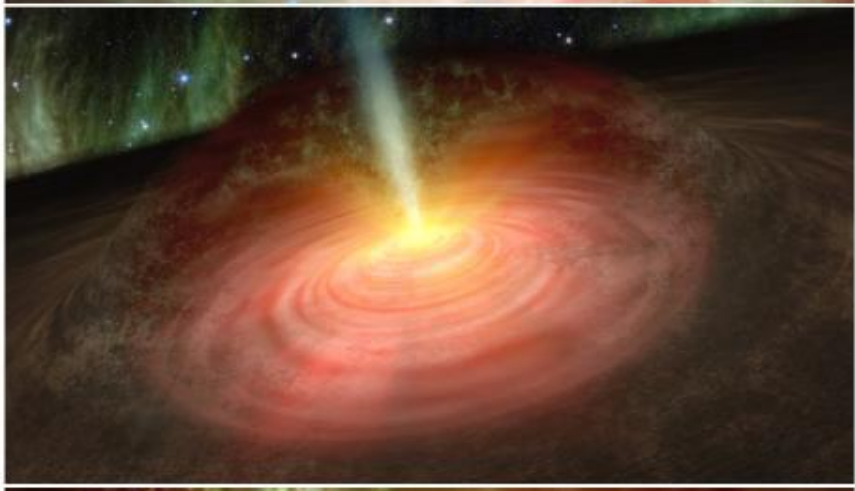

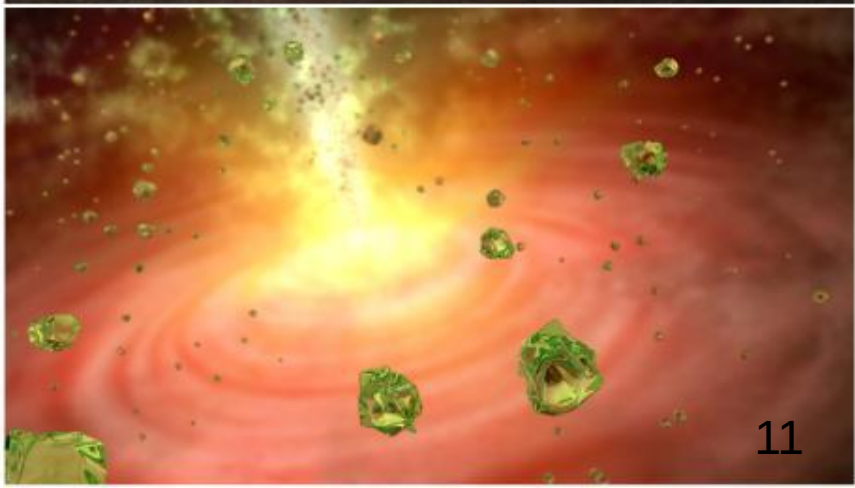

彗星内の結晶質シリケイトの問題

分子雲

氷　：　非晶質
岩石：　非晶質

彗星

氷　：　非晶質
岩石：　非晶質 ＋ 結晶質

← 低温保存物と
高温生成物が
共存している！

非晶質 → 結晶 --- 加熱で変性 (annealing)

氷　：~70K
岩石：~1000K

C/2002 V1(NEAT)彗星
内にある
岩石質微粒子
のスペクトル

シリケイト結晶
が存在！

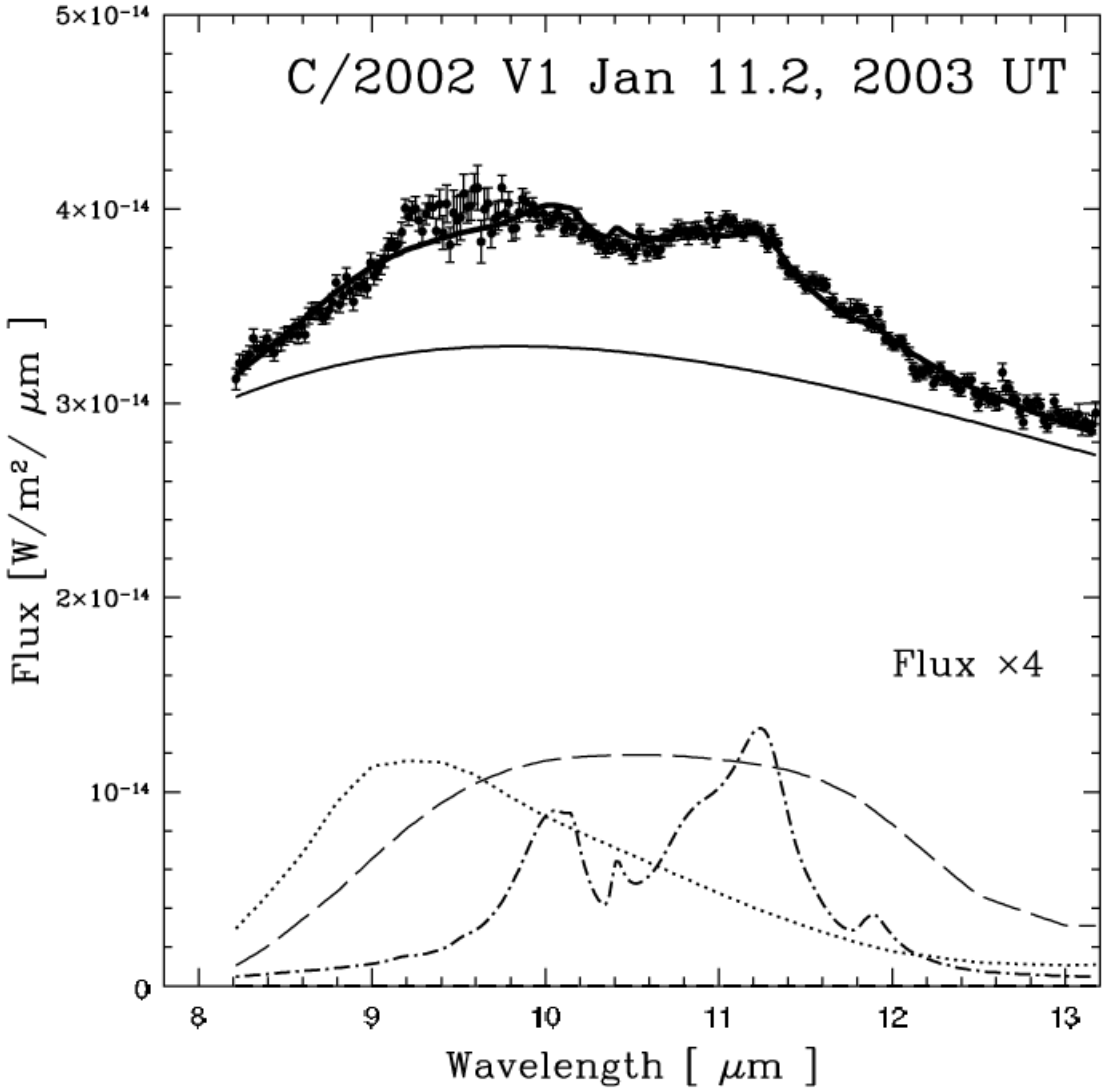

“Star Dust”プロジェクト

Wild2彗星の軌道

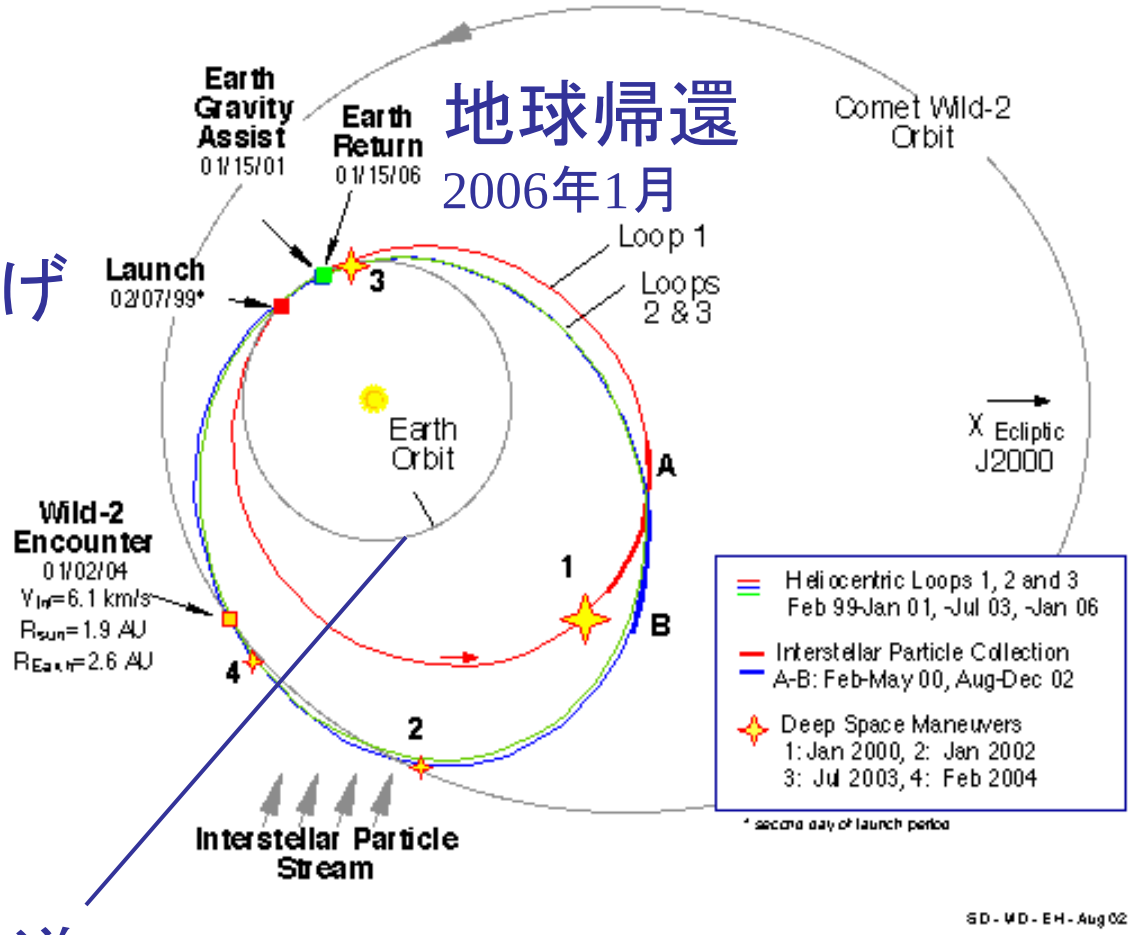

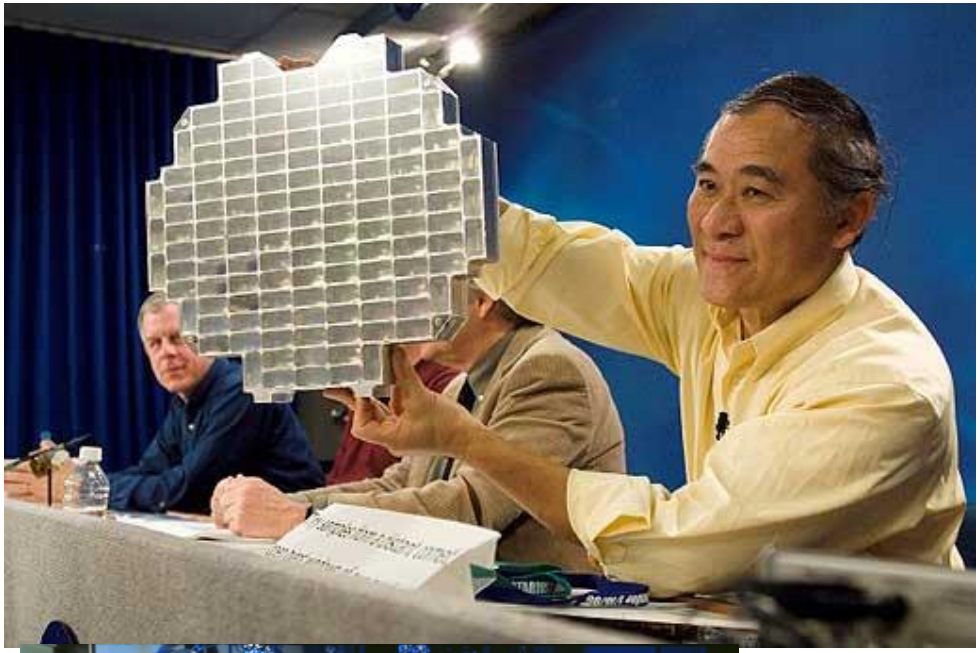

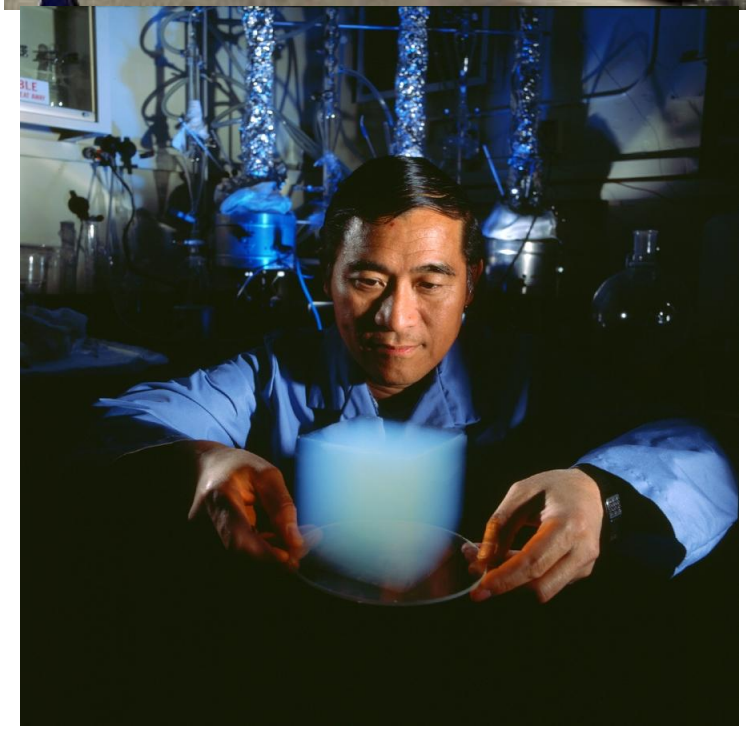

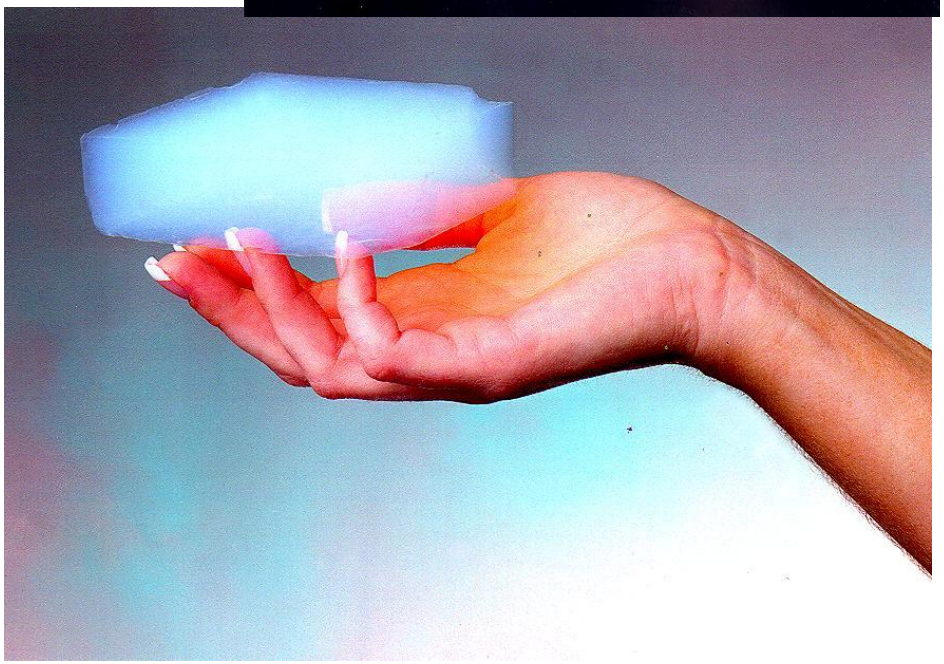

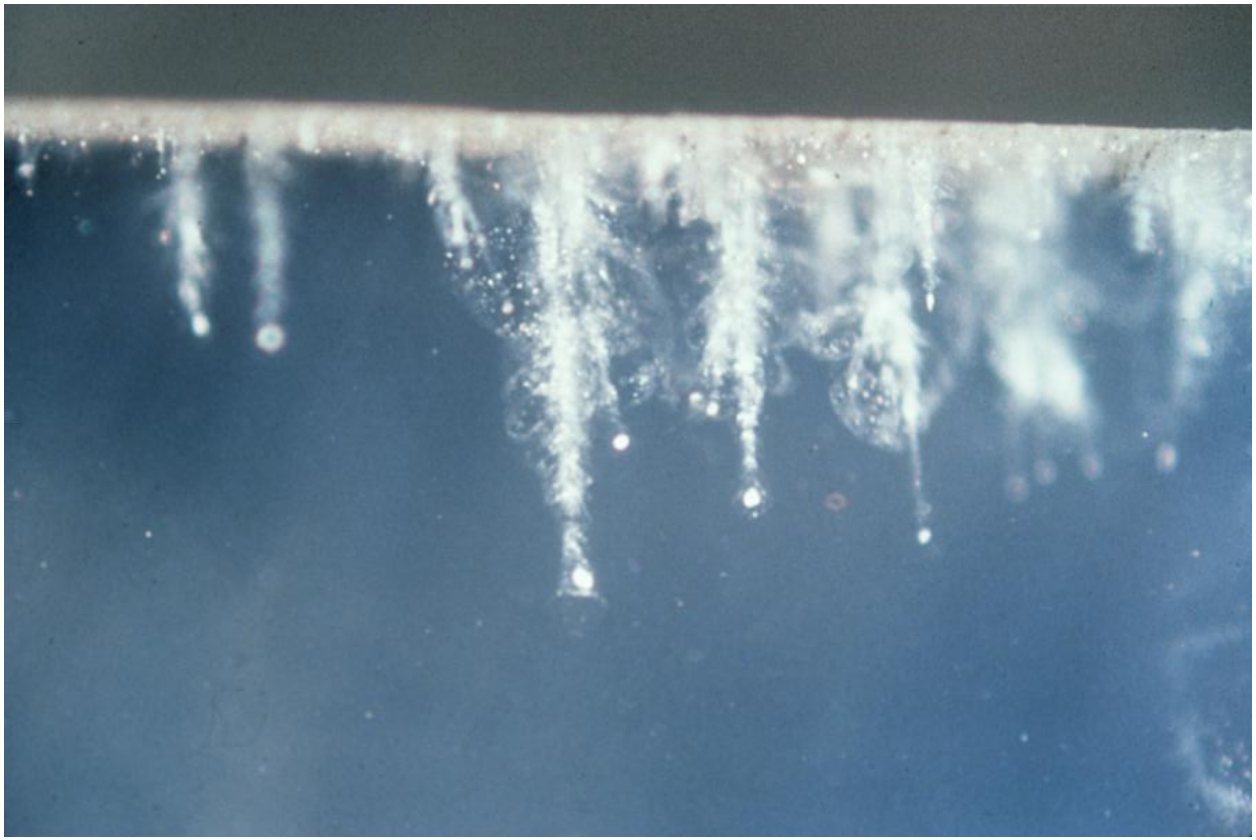

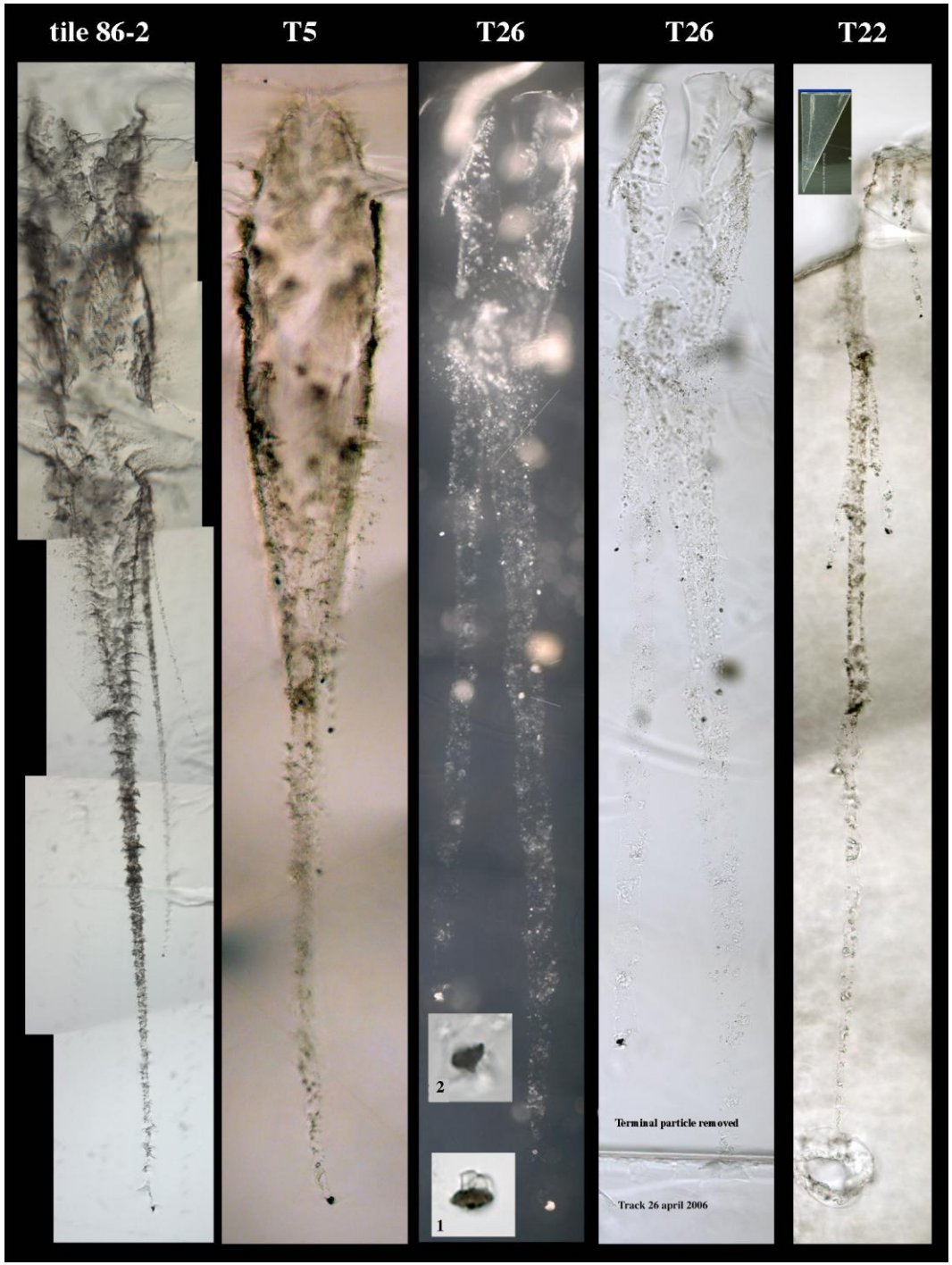

CAIやコンドリュールのような粒子がある！

結晶質シリケイトの混入

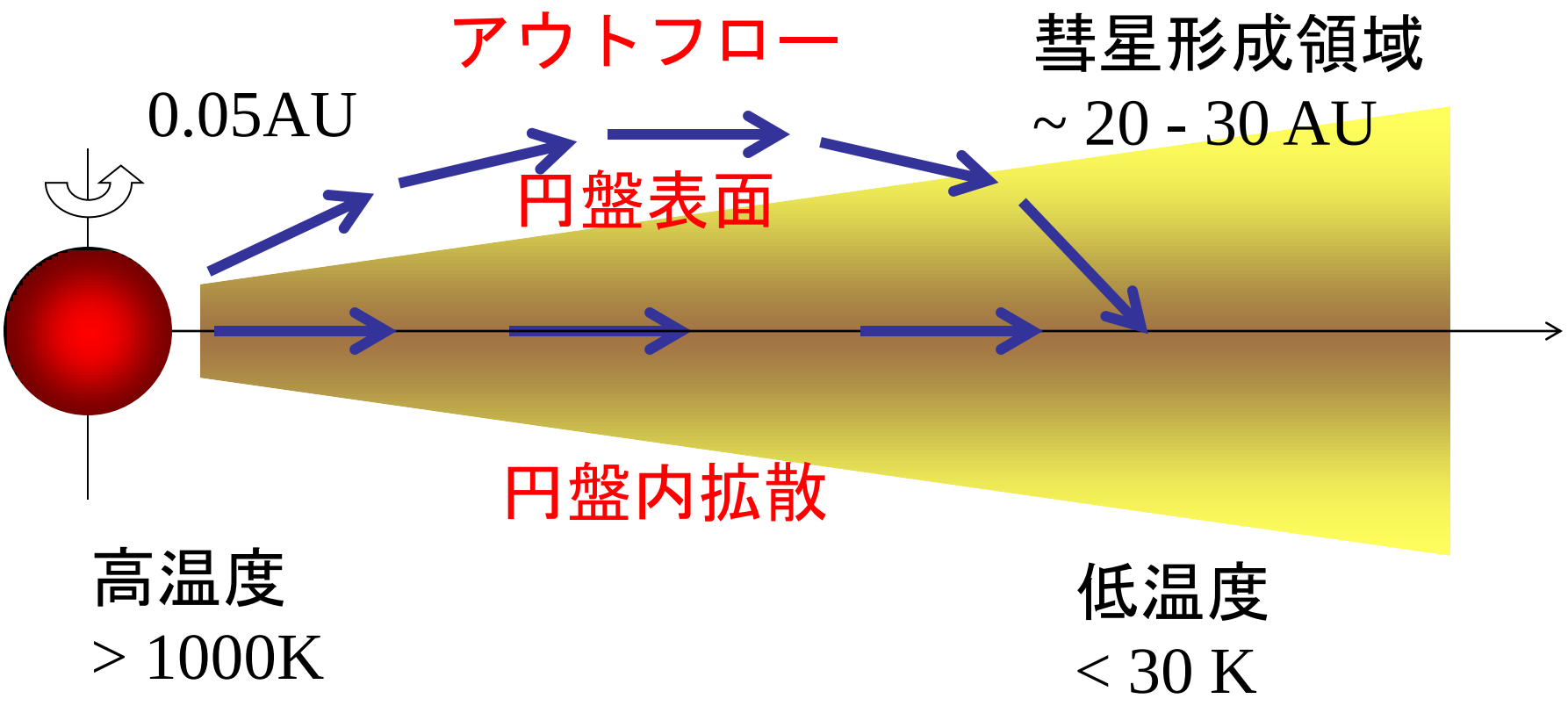

- 太陽近傍で結晶化した固体微粒子が外に運ばれた？
- 太陽系内物質循環？

氷は非晶質！

C/2002 T7 (LINEAR)彗星

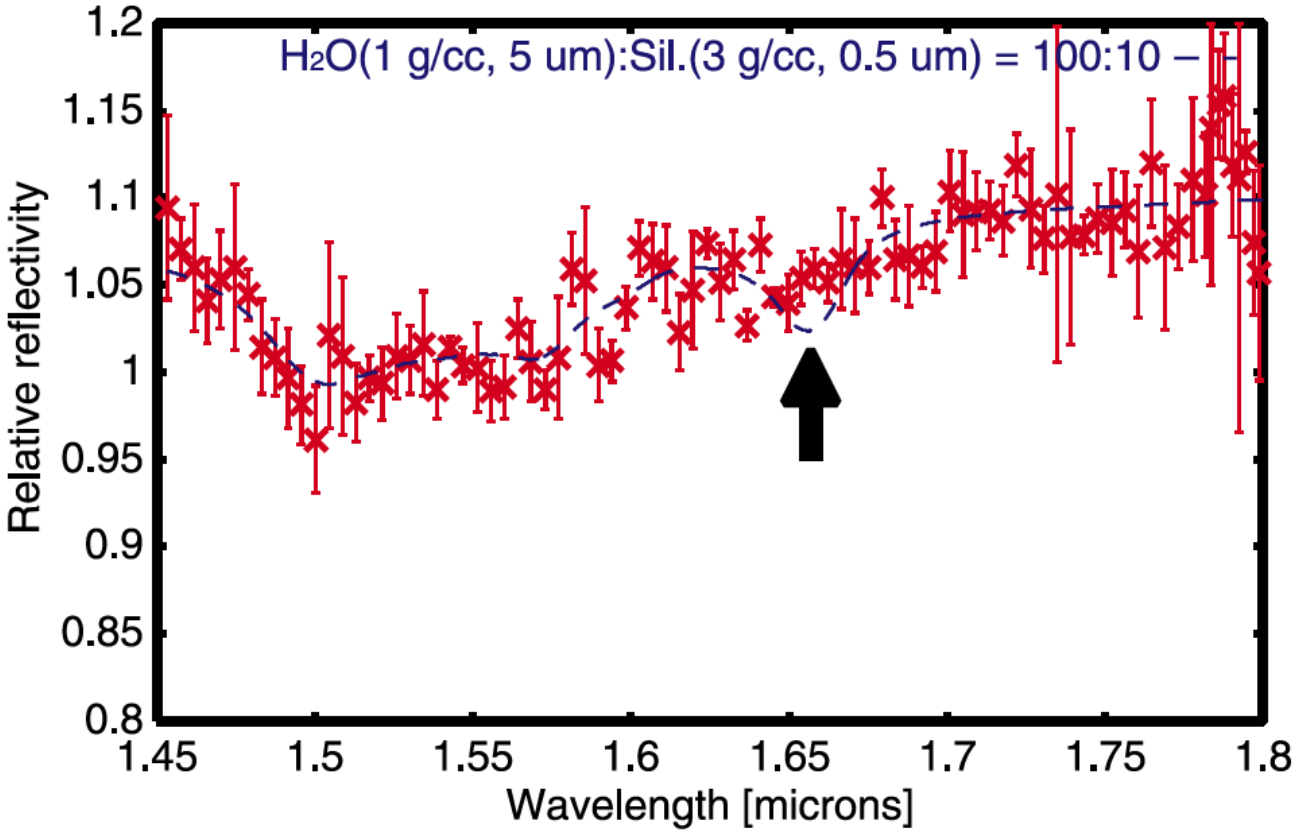

FIG. 3.—Close-up of Fig. 2 in the *H* band. The absence of the 1.65 μm absorption feature of crystalline ice may indicate that the cometary ice was in an amorphous state.

Kawakita et al. 2004

Hale-Bopp 彗星

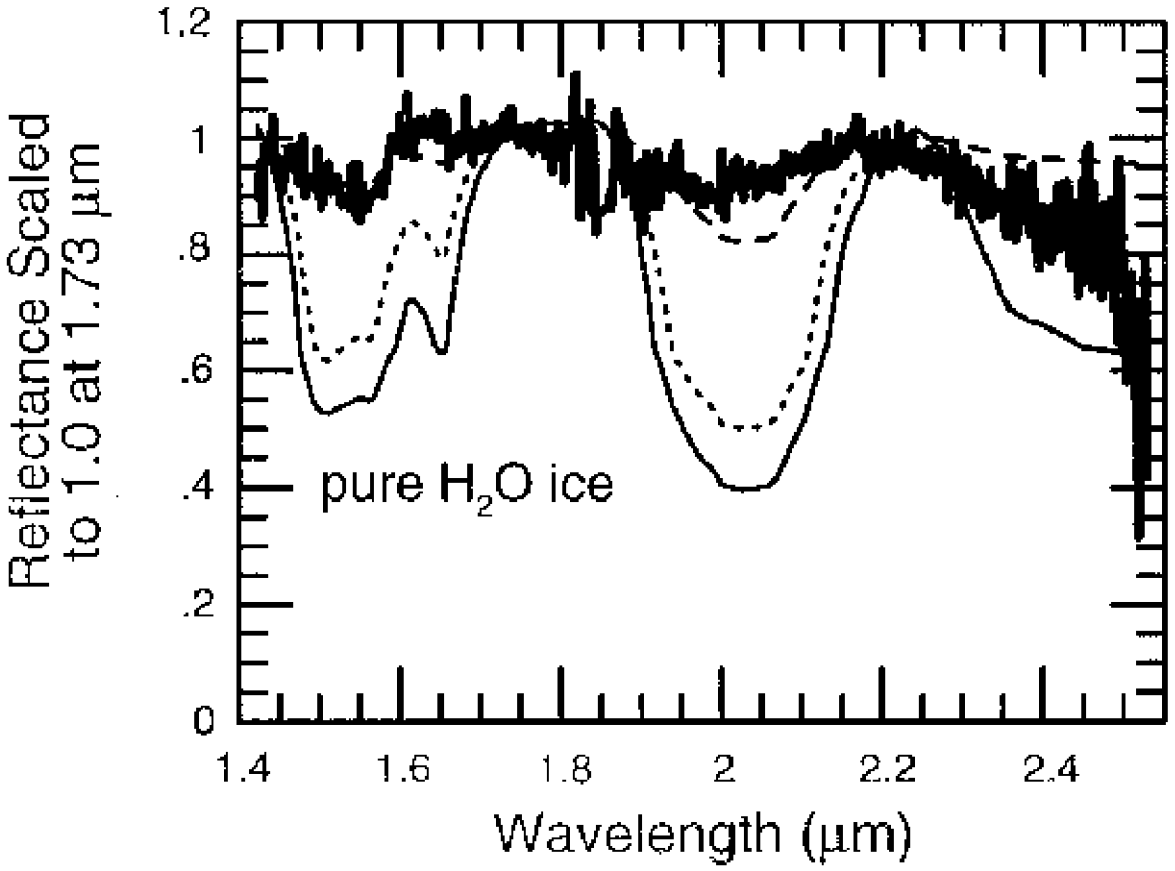

FIG. 3. Comet Hale-Bopp data (heavy solid line) compared with the reflectance calculated for water ice having grain diameters of 1 cm (dashed line), 5 cm (dotted line), and 10 cm (thin solid line).

Davies et al. 1997

低温で凍る(蒸発する)ものが含まれている

H_2O　-120℃ (絶対温度 150K)

CO　-248℃ (絶対温度 25K)

N_2　-251℃ (絶対温度 22K)

彗星の「氷」はいつ凍ったか？

分子雲中
(相対的に“高温”)

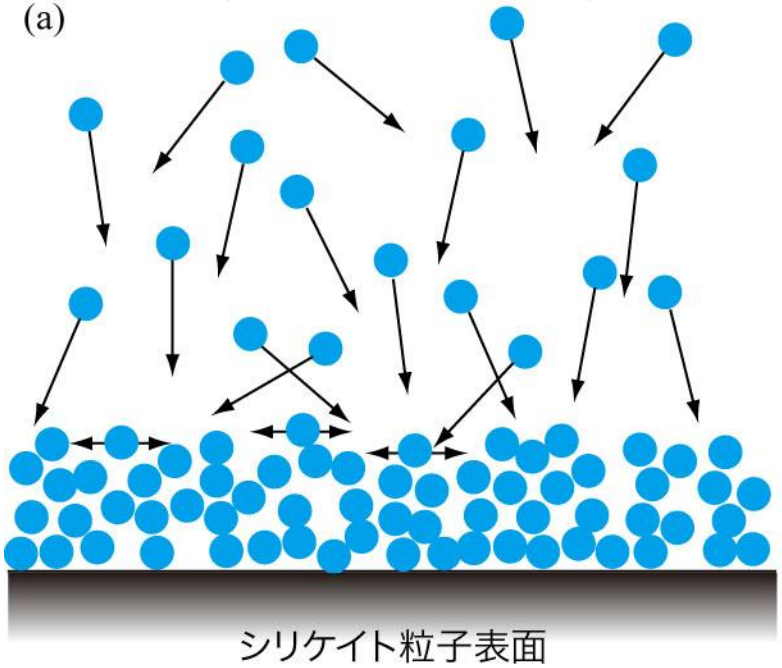

非晶質氷ができる

原始惑星系円盤中
(相対的に“低温”)

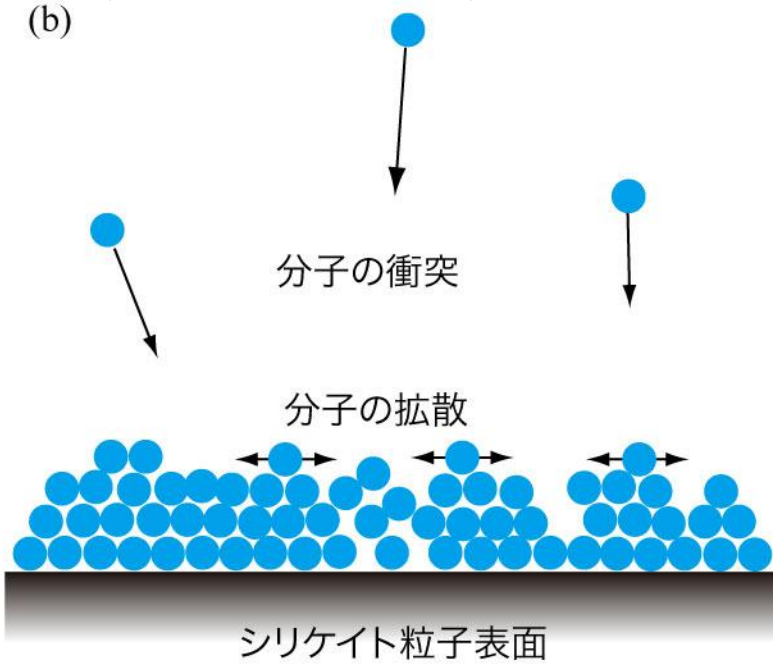

結晶質氷ができる

Kouchi et al. 1994

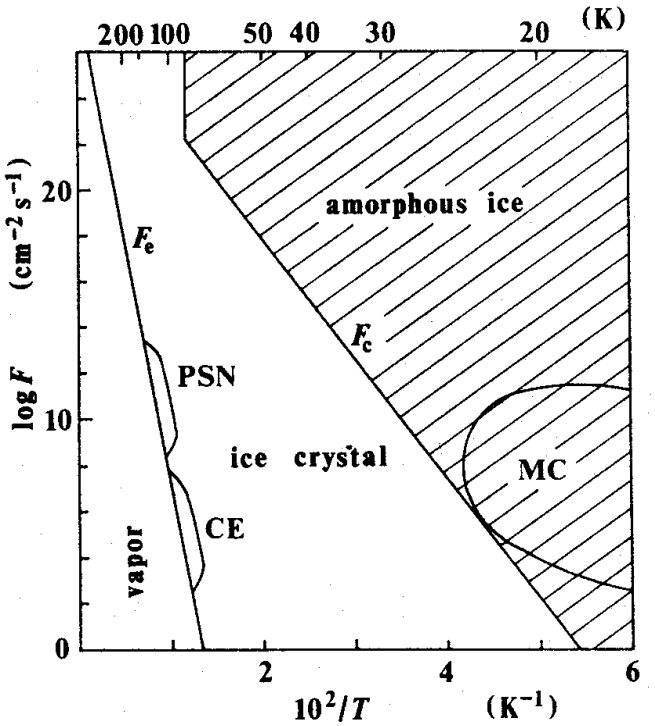

Fig. 6. Crystallinity of ices in astrophysical sites. F_c^* is the critical flux, and t_c is put 10^7 years. In upper abscissa, time scale for crystallization is shown. PSN, CE and MC denote the primordial solar nebula, circumstellar envelope and molecular cloud, respectively

is formed at the condensation because of $F < F_c$. Our conclusion is consistent with the experimental results obtained by

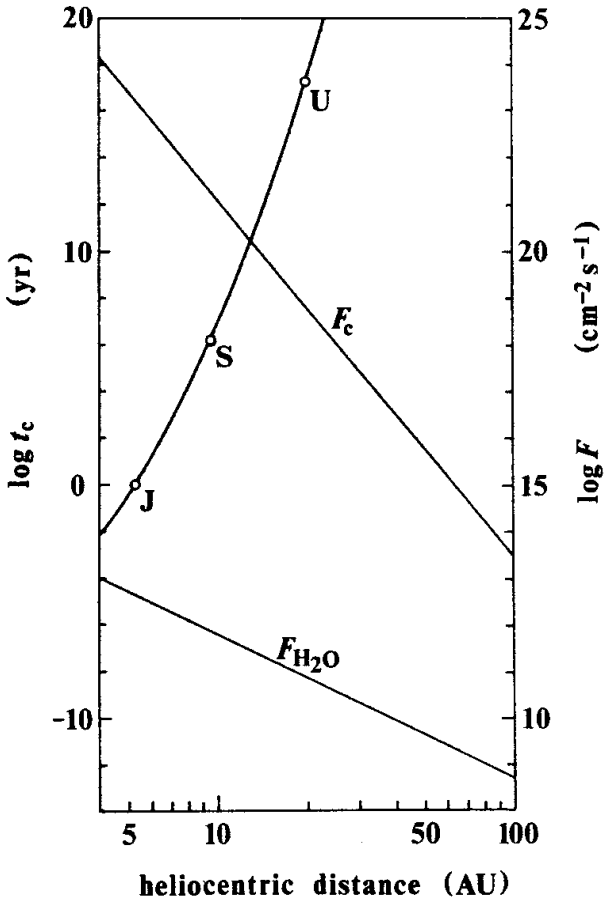

Fig. 8. Crystallization time scale t_c of amorphous ice in the primordial solar nebula (the left ordinate). The arrows labeled by J, S, U, ... indicate the present heliocentric distance of Jupiter, Saturn, Uranus, ... Flux of H_2O molecules F_{H_2O} for the case of recondensation also shown together with the critical flux F_c (the right ordinate)

彗星の氷は,
分子雲中で凍ったらしい

太陽よりも古い！

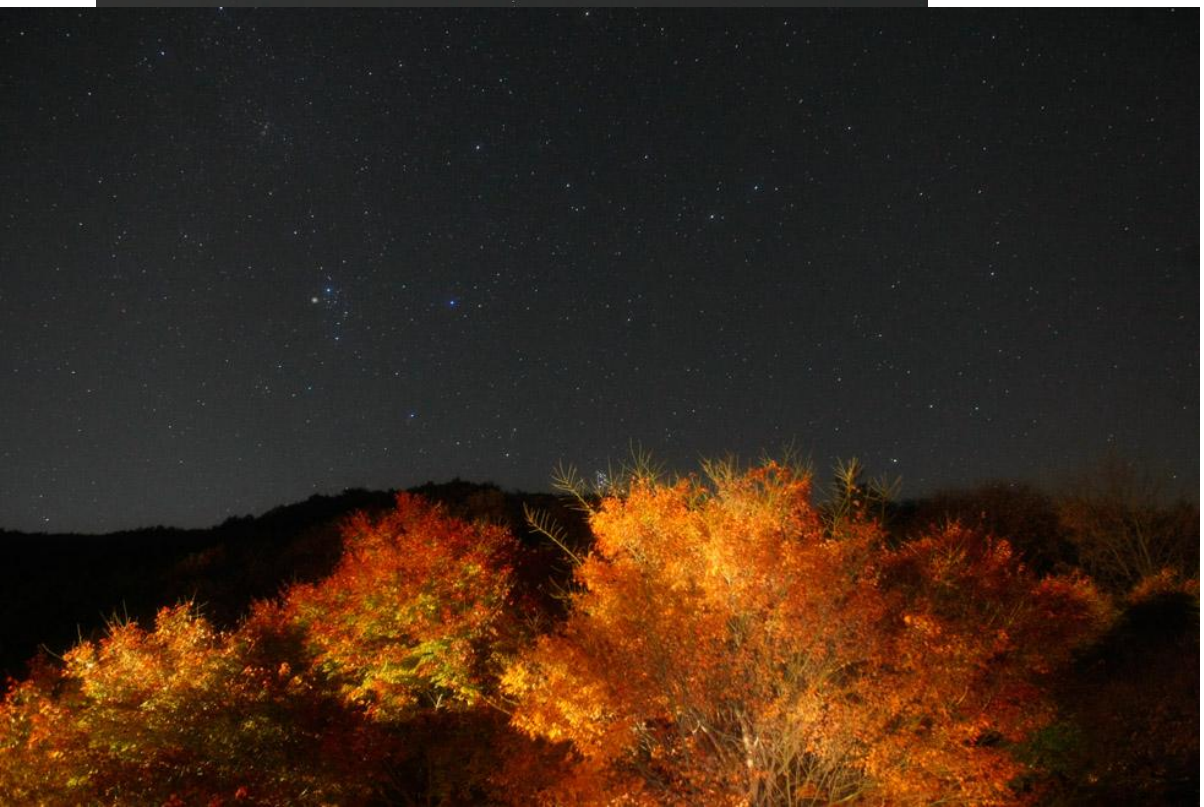

結晶質シリケイトの混入

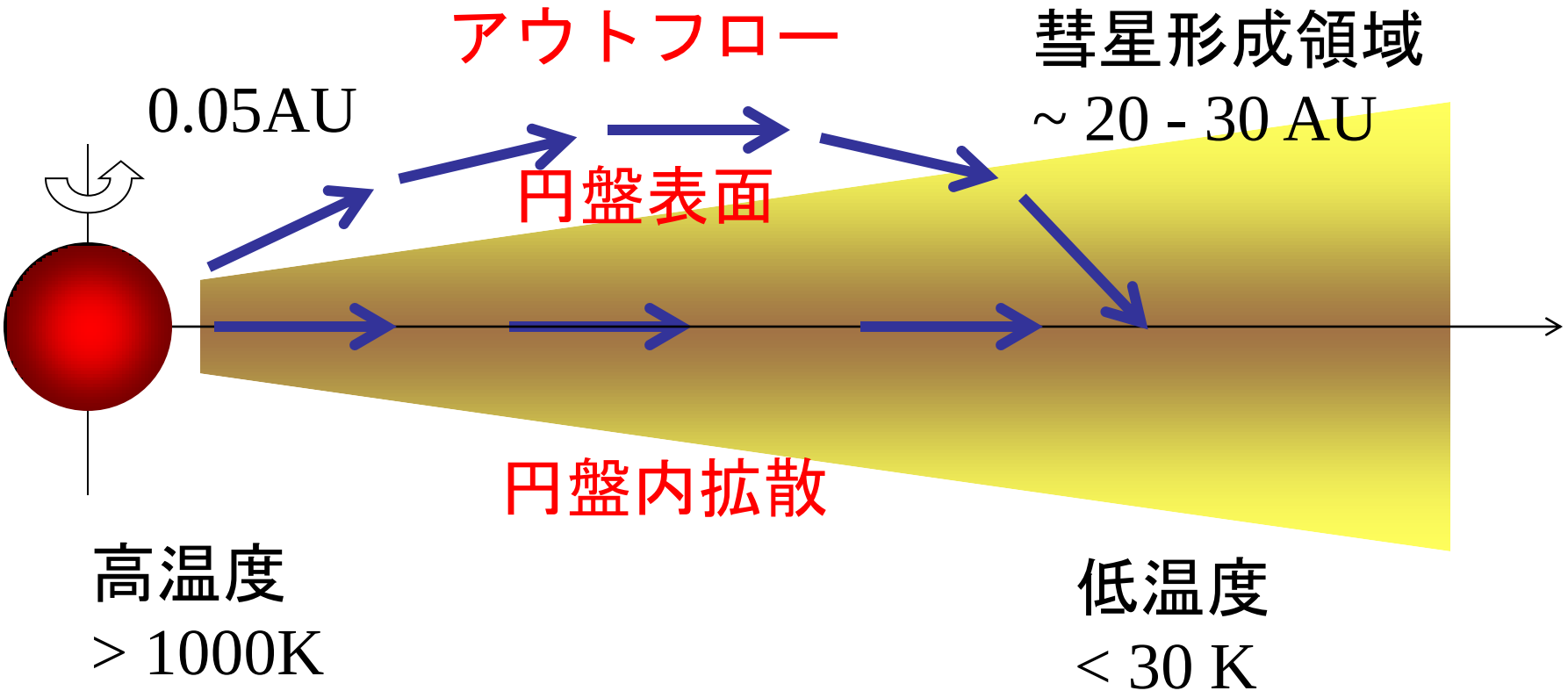

- 太陽近傍で結晶化した固体微粒子が外に運ばれた？
- 太陽系内物質循環？

Honda et al. 2008

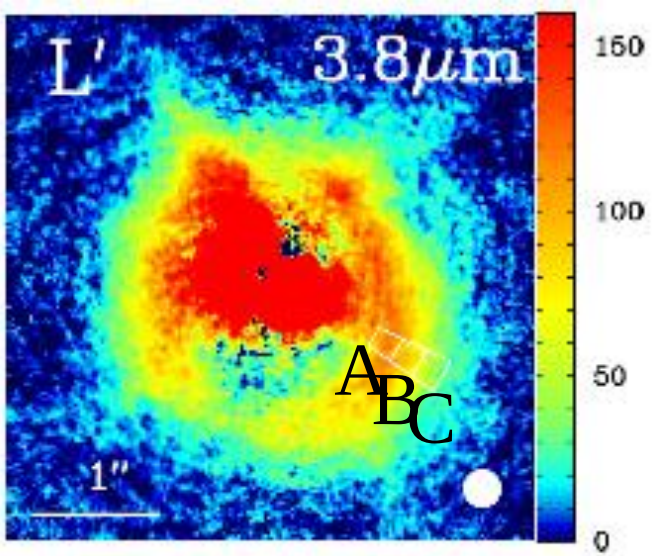

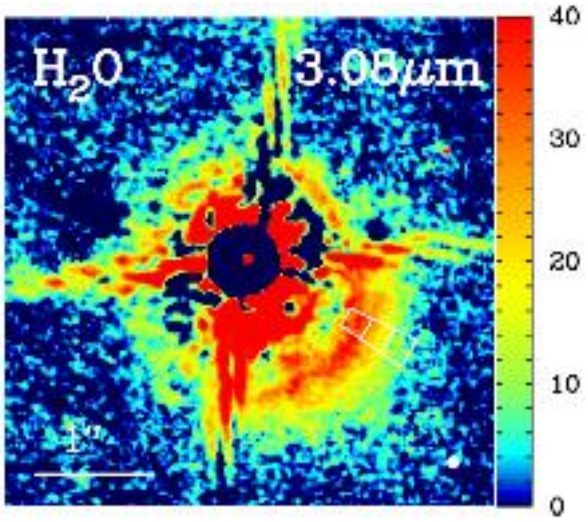

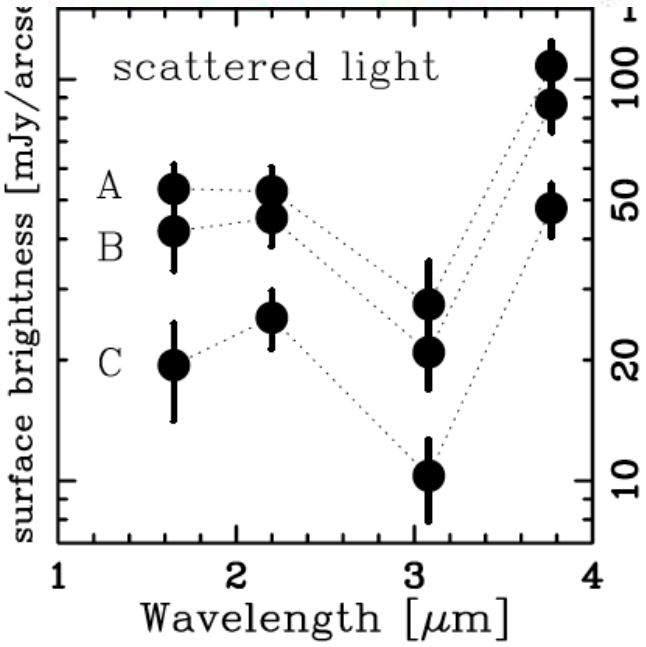

天体：HD142527

原始惑星系円盤の表面に
氷粒子があることを確かめた
初めての観測

ダストの運動

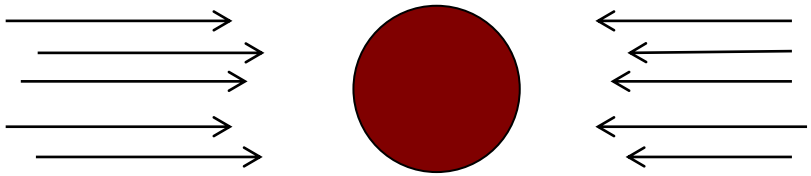

a：半径

l：ガスの
平均自由行程

$$F_{\rm drag} \approx \begin{cases} \dfrac{4\rho}{3} a^2 \rho_g c_s \left(v_g - V_d \right) & l > a \\ 3\rho l a \rho_g c_s \left(v_g - V_d \right) & l < a \end{cases}$$

分子流：Epstein則

流体：　Stokes則 ($Re < 1$)

$$\mathrm{Re} = \frac{a \left| v_g - V_d \right|}{\nu}$$

$$l = 1/n\sigma = 1.4 \text{ cm } (r = 1\text{AU of MMSN})$$
$$= 130 \text{ cm } (r = 5.2\text{AU of MMSN})$$

$$\sigma = 2 \times 10^{-15} \text{ cm}^2$$

相対速度がなくなるタイムスケール：stopping time

たとえば

$$m\frac{d\left(V_d - v_g\right)}{dt} = F_{\rm drag} = -\frac{4\rho}{3}a^2 r_g c_s \left(V_d - v_g\right) \qquad (l > a;\ \text{Epstein則のとき})$$

$$V_d - v_g = \left(V_d - v_g\right)_0 \exp\left[-t / t_s\right]$$

stopping time $\quad t_s = \dfrac{a r_s}{c_s\left(r_g + r_d\right)} \qquad l > a$：Epstein則

$$t_s = \frac{9}{4}\frac{a^2 r_s}{l c_s\left(r_g + r_d\right)} \qquad l < a$$：Stokes則

例えば，　@ 1AU

$$t_s = 7\times 10^3 \left(\frac{a}{1\,\text{mm}}\right)\text{sec} \qquad t_s = 3.6\left(\frac{a}{1\ \text{m}}\right)^2\ \text{yr}$$

MMSN at 1 AU

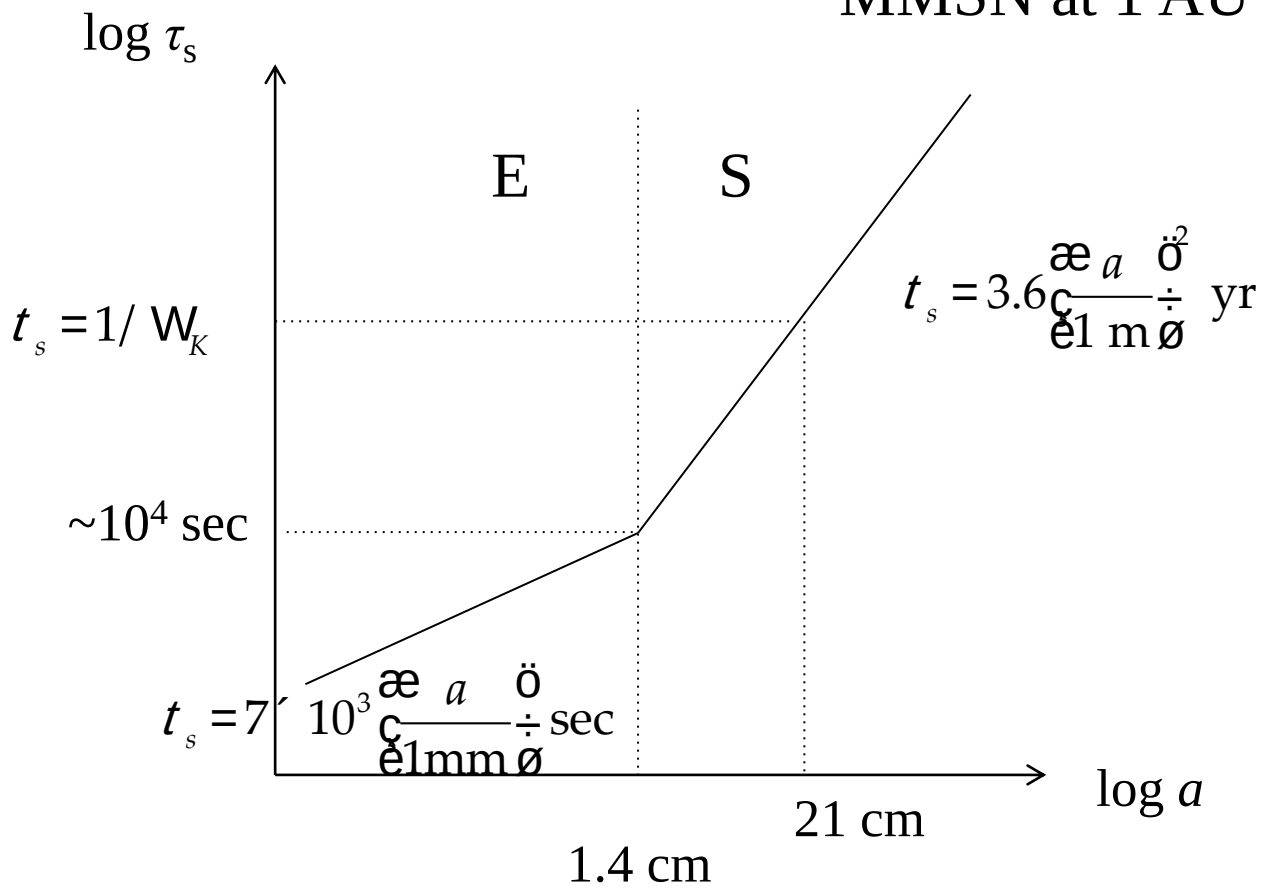
log τ_s
E
S
$t_s = 1/\Omega_K$
$t_s = 3.6 \left(\frac{a}{1\ \mathrm{m}}\right)^2$ yr
$\sim 10^4$ sec
$t_s = 7 \times 10^3 \left(\frac{a}{1\mathrm{mm}}\right)$ sec
log a
21 cm
1.4 cm

r方向の運動方程式

ガス

$$\frac{\partial v_{g,r}}{\partial t} + v_{g,r}\frac{\partial v_{g,r}}{\partial r} - \frac{v_{g,j}^2}{r} = -\frac{1}{r}\frac{\partial p}{\partial r} + 2\Omega_K v_{g,j} - \gamma_d A\left(v_{g,r} - V_{d,r}\right)$$

ダスト

$$\frac{\partial V_{d,r}}{\partial t} + V_{d,r}\frac{\partial V_{d,r}}{\partial r} - \frac{V_{d,j}^2}{r} = 2\Omega_K V_{d,j} - \gamma_g A\left(V_{d,r} - v_{g,r}\right)$$

圧力勾配 / 重力×2

$$h = -\frac{1}{2}\left(\frac{1}{r}\frac{\partial p}{\partial r} \Big/ r\Omega_K^2\right) = -\frac{1}{2}\left(\frac{c_s}{V_K}\right)^2 \frac{\partial \ln p}{\partial \ln r}$$

$$= 1.8\times 10^{-3}\left(\frac{r}{1\ \mathrm{AU}}\right)^{1/2} \quad \text{(MMSN)}$$

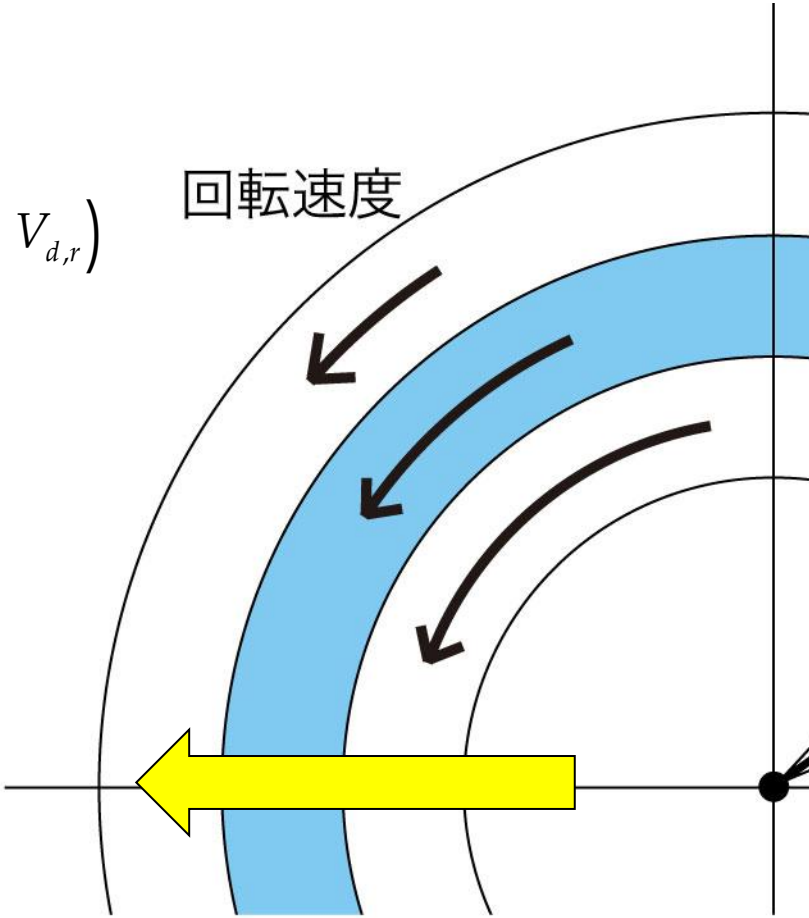

定常解

Nakagawa et al. 1986

$$V_{d,r} = -\frac{1}{1+r_d/r_g}\frac{2g}{1+g^2}\eta V_K$$

$$V_{d,j} = -\frac{1}{1+r_d/r_g}\frac{1}{1+g^2}\eta V_K$$

$$v_{g,r} = \frac{r_d/r_g}{1+r_d/r_g}\frac{2g}{1+g^2}\eta V_K$$

$$v_{g,j} = \left(\frac{r_d/r_g}{1+r_d/r_g}\frac{1}{1+g^2} - 1\right)\eta V_K$$

$$v_{g,z} - V_{d.z} = -\frac{\Omega_K^2}{A r_g} z$$

$$g = t_s \Omega_K$$

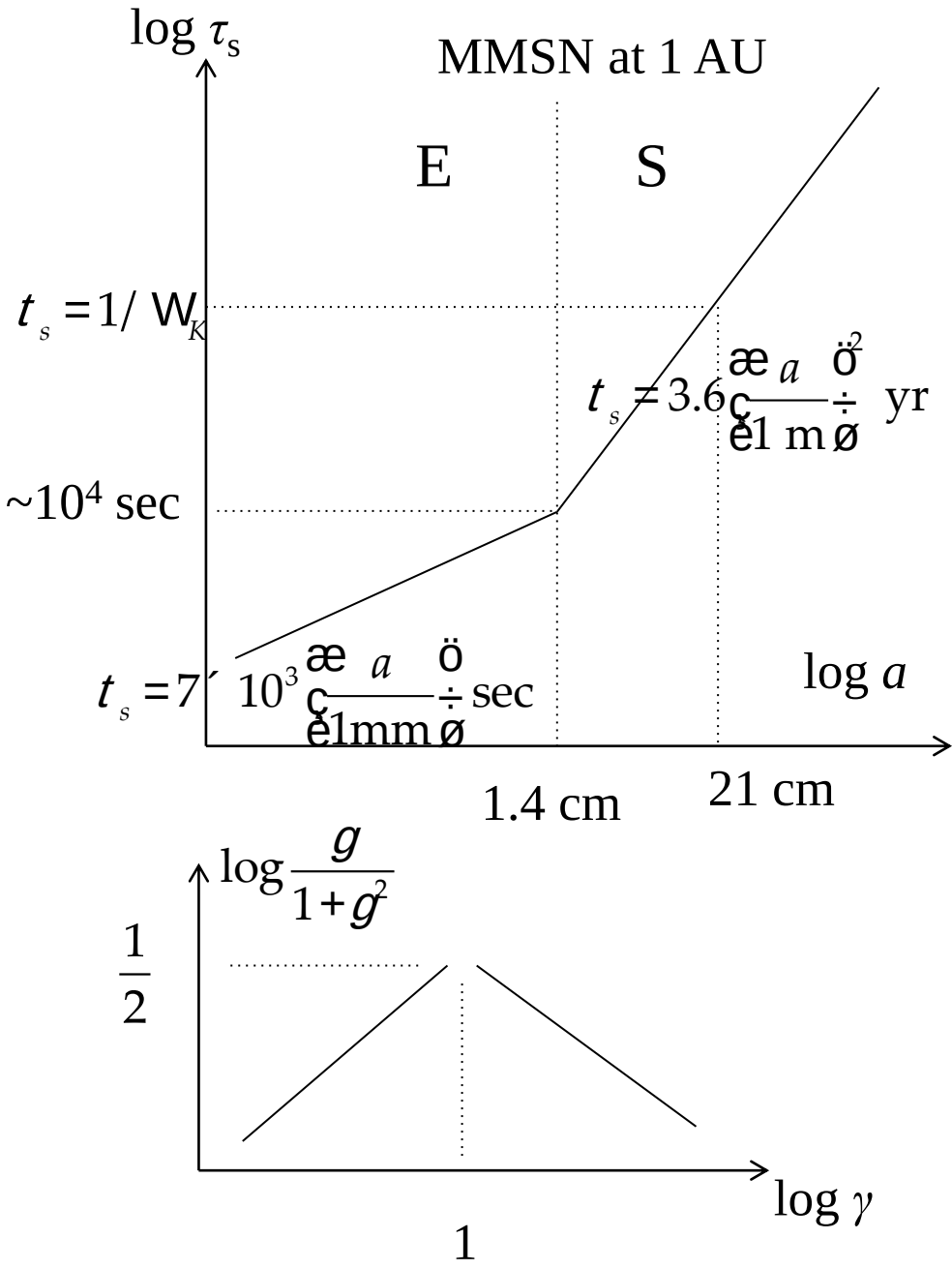

MMSN, @ 1AU　　a = 21 cm

$$V_{d,r} = -\frac{1}{1+r_d/r_g}\frac{2g}{1+g^2}\eta V_K = -1.8\times 10^{-3} V_K$$

ダスト粒子のr方向
最大移動速度

$$t_{\rm drift} = \frac{r}{|V_{d,f}|} = \frac{r}{\eta V_K} = \frac{1}{2\pi\eta} T_K = 90 \text{ yr}$$

ダスト粒子のr方向
最小移動時間

ダストはガスの圧力勾配
の逆方向に移動

ダスト粒子の衝突合体

電磁気的な力：
ファンデルワールス力
分子間力

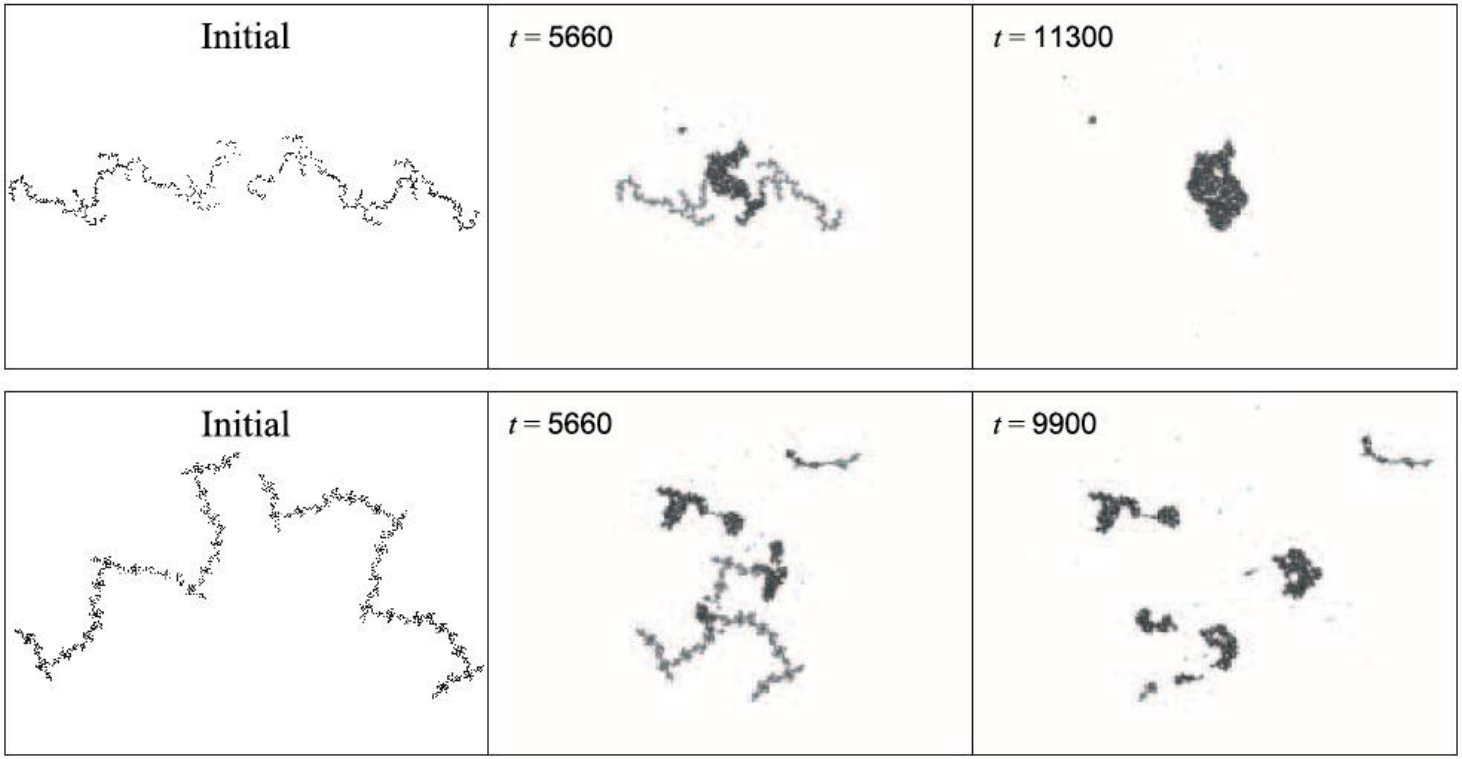

~ 0.1 mm

Wada *et al*. 2007

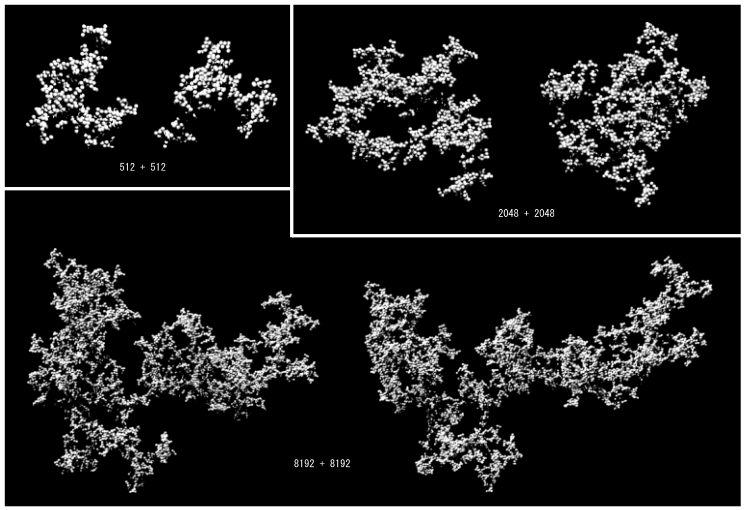

FIG. 1.—Examples of initial BCCA clusters. These aggregates collide with each other horizontally. Each aggregate consists of 512, 2048, or 8192 identical particles.

Wada et al. 2008

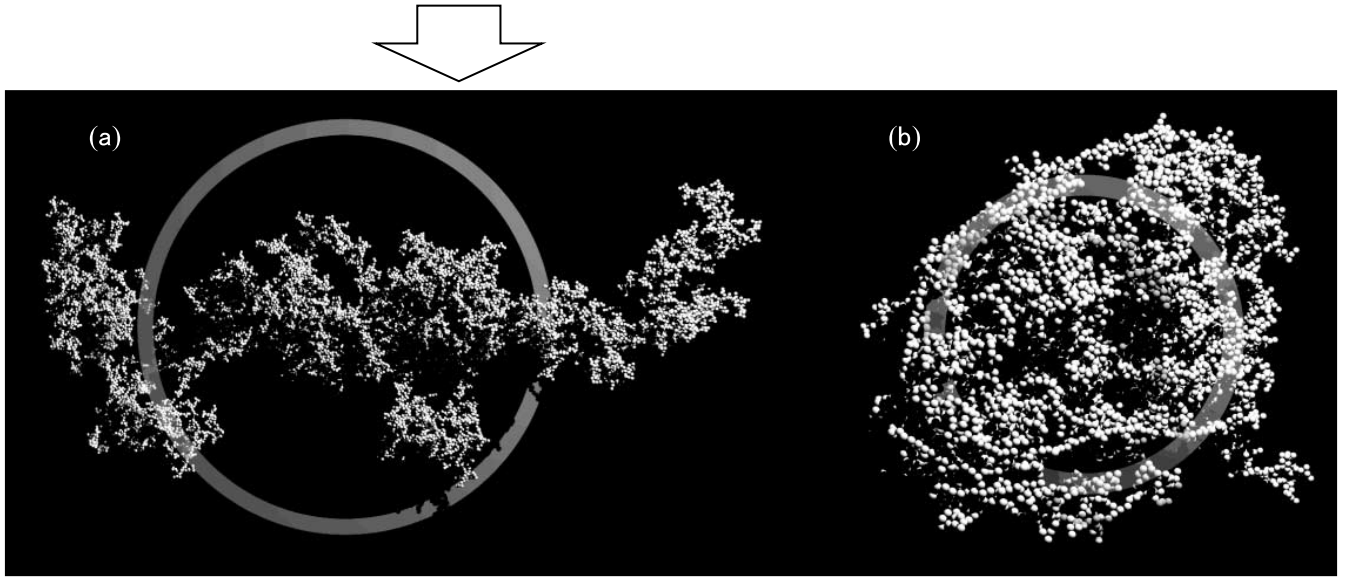

FIG. 3.—Examples of collisional outcomes: (*a*) no restructuring ($u_{\rm imp} = 0.024$ m s^{-1} and $E_{\rm imp} = 0.01E_{\rm roll}$) and (*b*) maximum compression ($u_{\rm imp} = 13$ m s^{-1} and $E_{\rm imp} = 0.19n_kE_{\rm roll}$). Both resultant aggregates are composed of 16,384 ice particles of 0.1 μm radius with $\xi_{\rm crit} = 8$ Å. The gray ring for each aggregate indicates the size of the gyration radius.

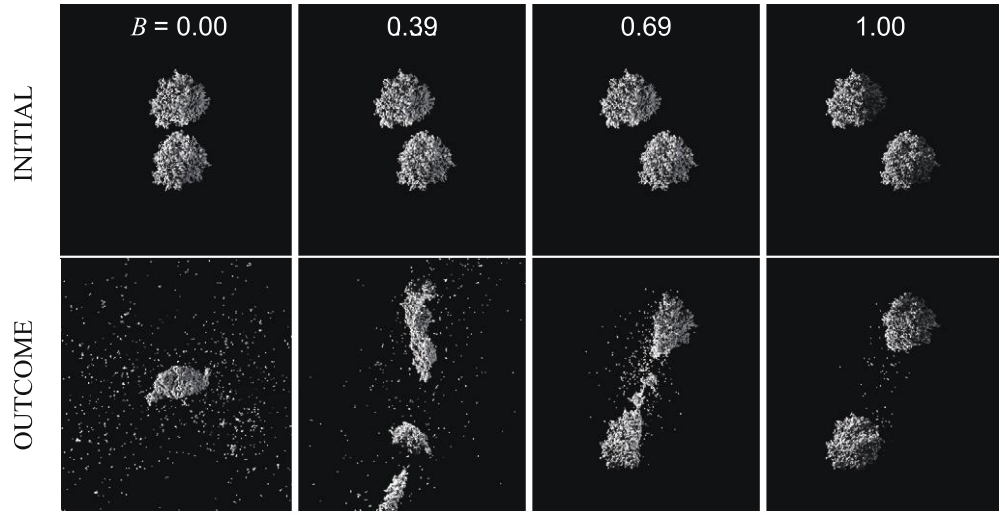

氷ダスト

$v > 50$ m/s
で破壊

Figure 2. Examples of collisional outcomes of BPCA clusters consisting of 8000 ice particles. Initial aggregates are shown in the upper panels and they collide with each other vertically (from left to right: $B = 0.00$, 0.39, 0.69, and 1.00, respectively). Collisional outcomes at a collision velocity of 70 m s^{-1} ($E_{\rm imp} = 42 N_{\rm total} E_{\rm break}$) are shown in the lower panels, corresponding to the upper initial conditions.

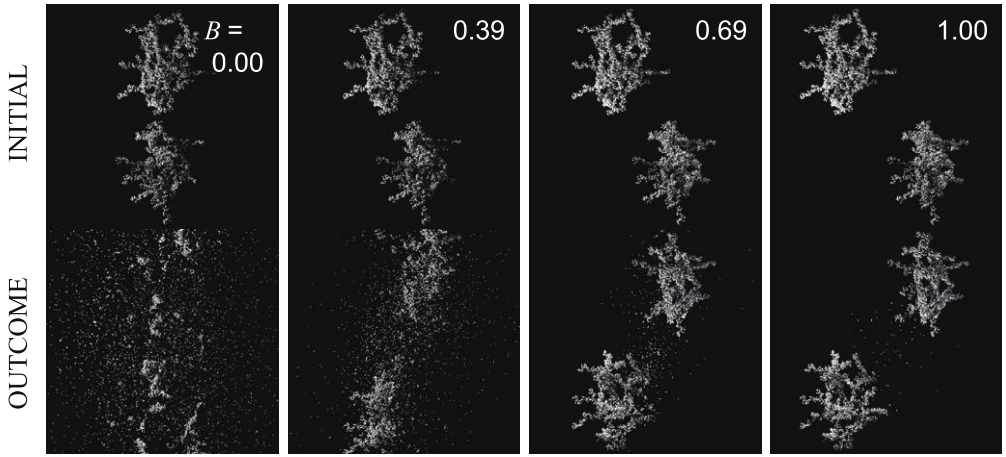

Figure 3. Same as Figure 2 but for BCCA clusters consisting of 8192 ice particles.

Wada et al. 2009

ダストの成長＆移動

Nakagawa et al. 1986

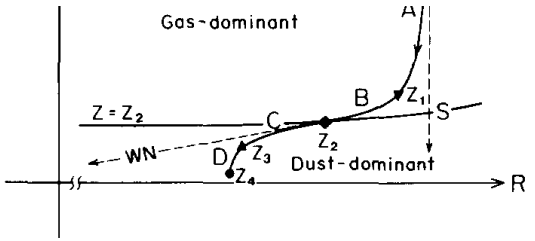

FIG. 1. A schematic illustration of the settling path in the RZ plane (solid curve). Z_0 (○) is the initial height and Z_4 (●) the final. Z_2 (◆) is the boundary height, dividing the settling process into the gas-dominant phase and the dust-dominant one. Z_1 (▼) and Z_3 (▲) are the heights of the turning points. The labels A, B, C, and D denote the settling phases from Z_0 to Z_1, from Z_1 to Z_2, from Z_2 to Z_3, and from Z_3 to Z_4, respectively. The dashed lines are the settling paths adopted in the previous studies by Safronov (S) and by Weidenschilling (W) and Nakagawa *et al.* (N).

path has two turning points at heights Z_1 and Z_3, where $dZ/dR = 1$. At a boundary height Z_2, the settling process is divided into two main phases, i.e., the gas-dominant phase and the dust-dominant phase.

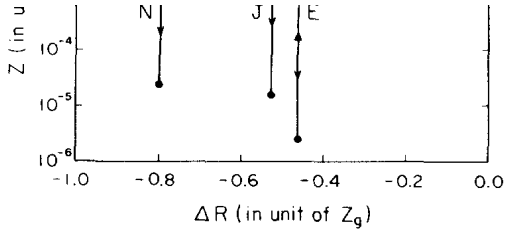

FIG. 2. Typical settling paths of dust particles in the Earth's (E), Jupiter's (J), and Neptune's (N) zones. Abcissa: the radial displacement, $\Delta R \equiv R - R_0$, in unit of the half-thickness of nebular gas, Z_g. Ordinate: the height from the equatorial plane, Z, in unit of Z_g. The symbols of ○, ▼, ◆, ▲, and ● represent the heights of Z_0, Z_1, Z_2, Z_3, and Z_4 in each zone, respectively. The portions with $Z_0 \geq Z \geq Z_1$ and with $Z_3 \geq Z \geq Z_4$ are nearly vertical and those with $Z_1 \geq Z \geq Z_3$ nearly radial.

III. SETTLING PATH

Although the steady velocity, V, found in the preceding section is the velocity of the *dust fluid*, it can be regarded as that of individual dust particles as long as $r < \tilde{r}$. In this

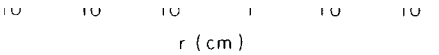

FIG. 3. Growth curves of dust particles. The typical radii of growing dust particles in the three zones E, J, and N are plotted as a function of the height, Z, in unit of Z_g. The symbols of ○, ▼, ◆, ▲, and ● represent the heights of Z_0, Z_1, Z_2, Z_3, and Z_4 in each zone, respectively.

ing in Section I). Mutual collisions can occur between dust particles with different sizes owing to the velocity difference in V_R and V_Z, which have a size dependence through the drag coefficient. The azimuthal velocity, V_ϕ, has no size dependence and brings about no contribution to the collisions.

Now we consider a representative dust particle. The mass of the dust particle, m, increases according to the growth equation

smaller than the settling time of other ones to be swept, t_s (see Appendix B); therefore, ρ_d does not increase appreciably during the collisions. Then, by an integration of Eq. (4.1), we obtain

$$r = r_0 + r_S\{1 - (Z/Z_0)\}, \qquad (4.2)$$

where r_S is given by Eq. (1.2). This relation is plotted in Fig. 3. Putting $Z = Z_1$ in Eq. (4.2), we find that the radii, r_1's, at the first turning point are 0.41, 0.28, and 0.025 cm in the Earth's, Jupiter's, and Neptune's

Okuzumi et al. 2012

氷ダスト，破壊なし モデル

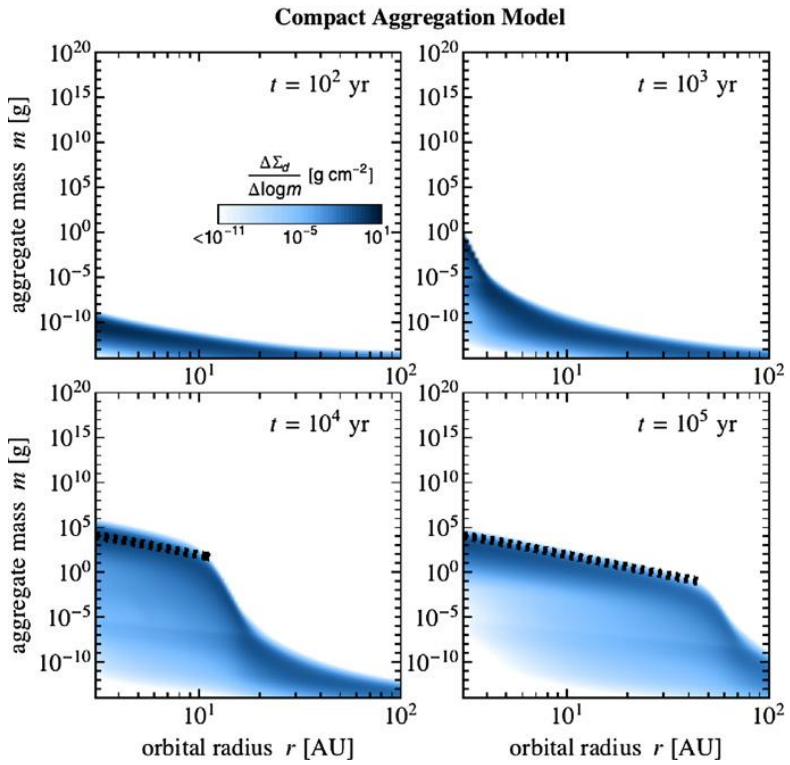

Figure 2. Aggregate size distribution $\Delta\Sigma_d/\Delta \log m$ at different times t for the compact aggregation model ($\rho_{\rm int} = 1.4\,{\rm g\,cm^{-3}}$) as a function of orbital radius r and aggregate mass m. The dotted lines mark the aggregate size at which Ωt_s exceeds 0.1.

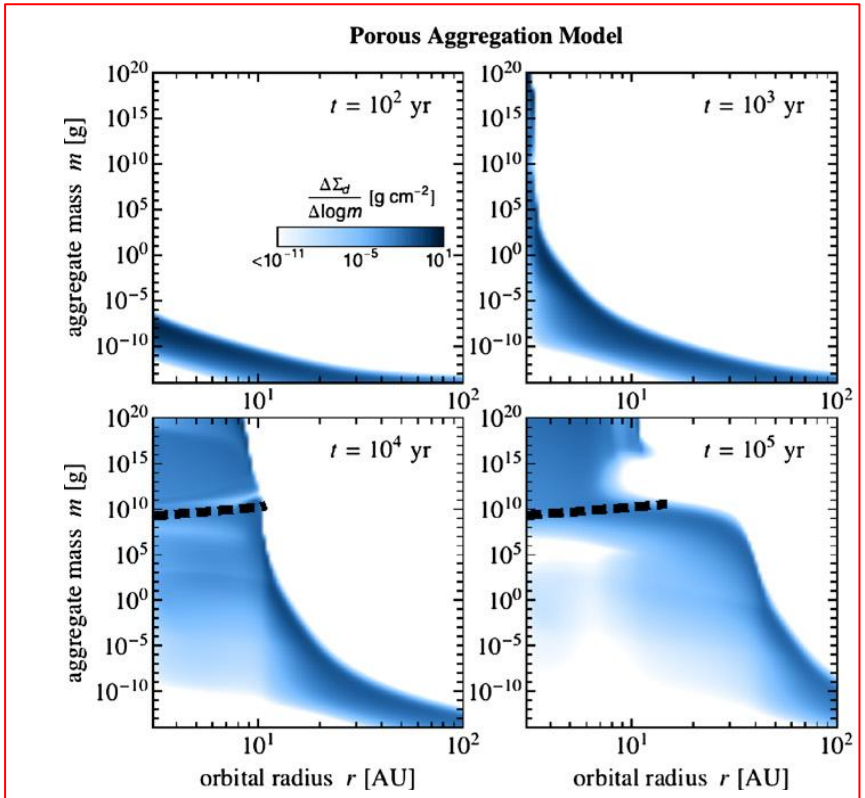

Figure 5. Aggregate size distribution $\Delta\Sigma_d/\Delta \log m$ (left four panels) and internal d
model as a function of orbital radius r and aggregate mass m. The dashed lines ma

Okuzumi et al. 2012

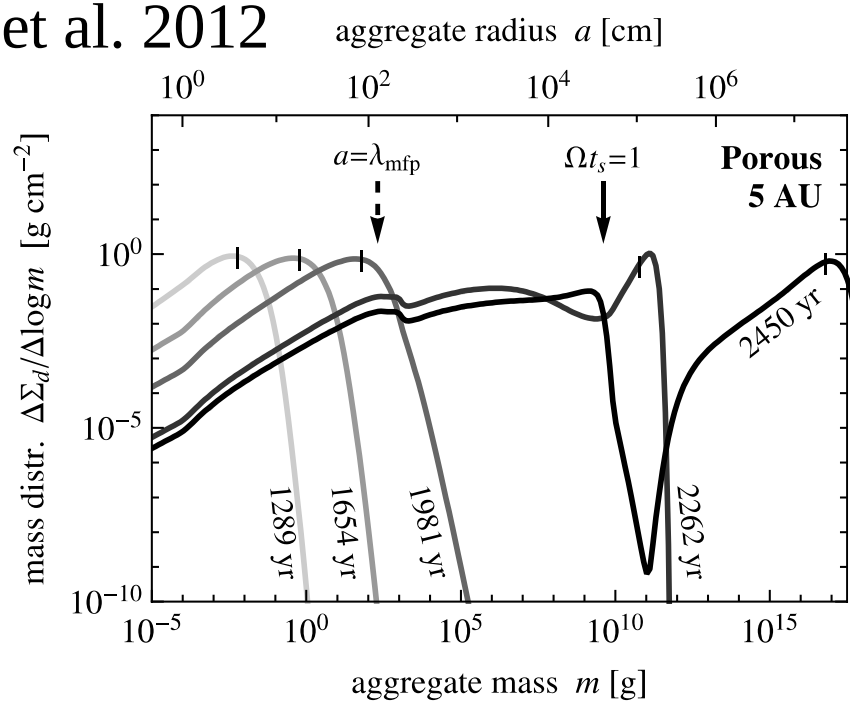

微惑星ができる！

- 破壊は大丈夫？
- 岩石微惑星は？

微惑星形成過程の問題

- 連続合体成長モデル
  大丈夫？

- 重力不安定モデル
  重力不安定が起こるか？

ダスト層の形成

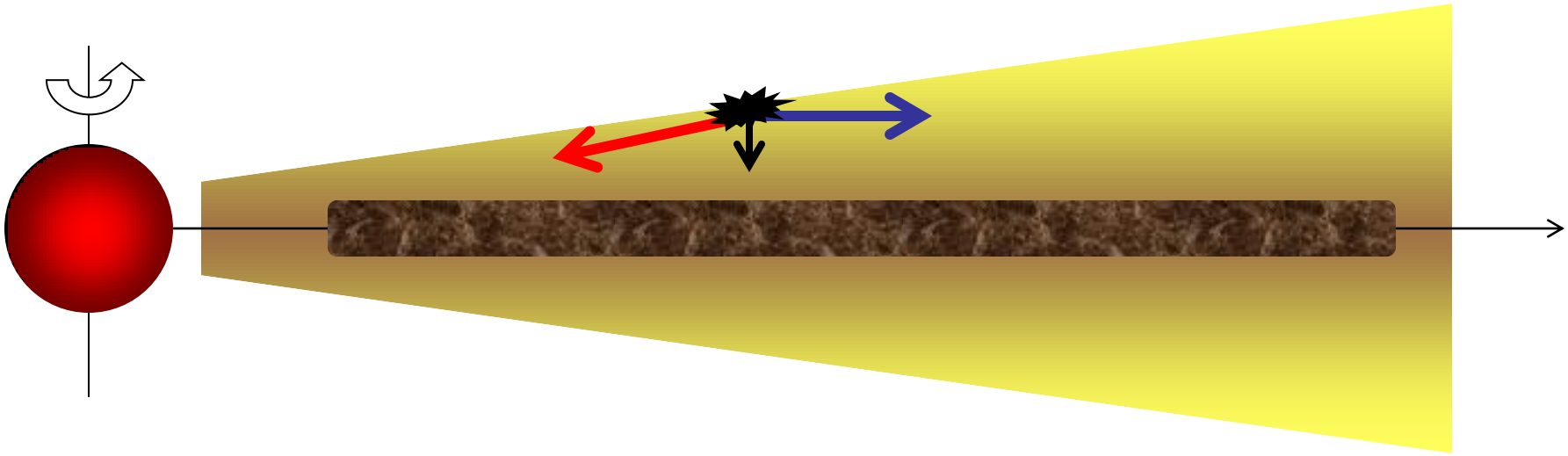

・固体微粒子(ダスト)が“沈殿”
・大きさ 1 mm - 1 cm程度

「重力不安定」微惑星形成モデル

Goldreich & Ward 1973

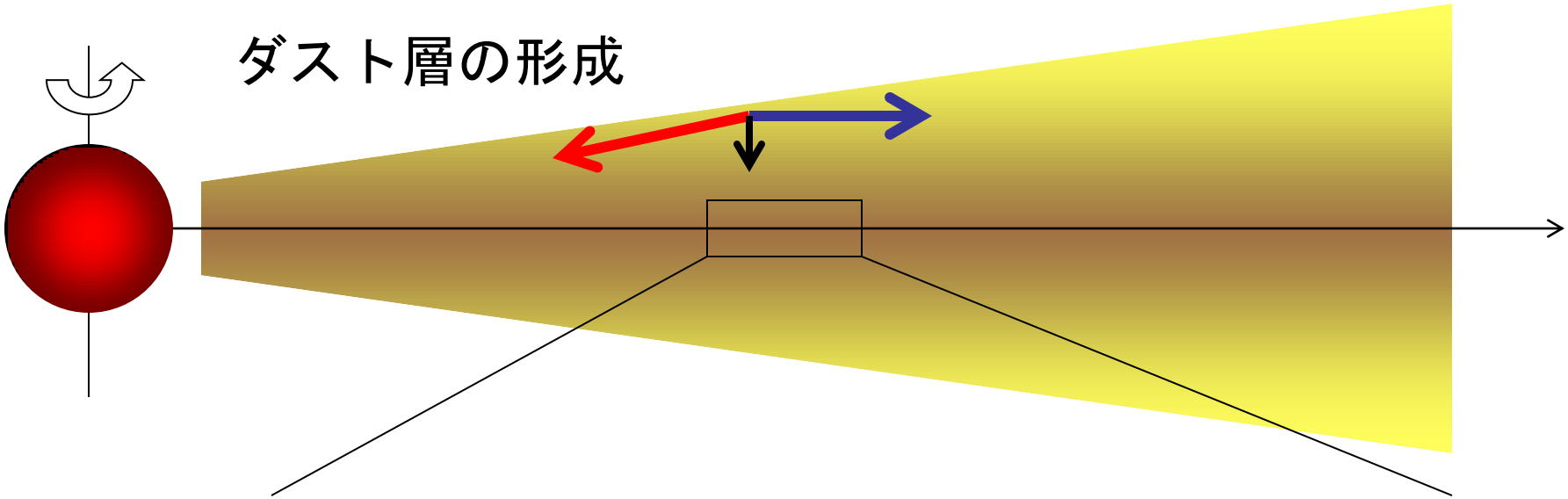

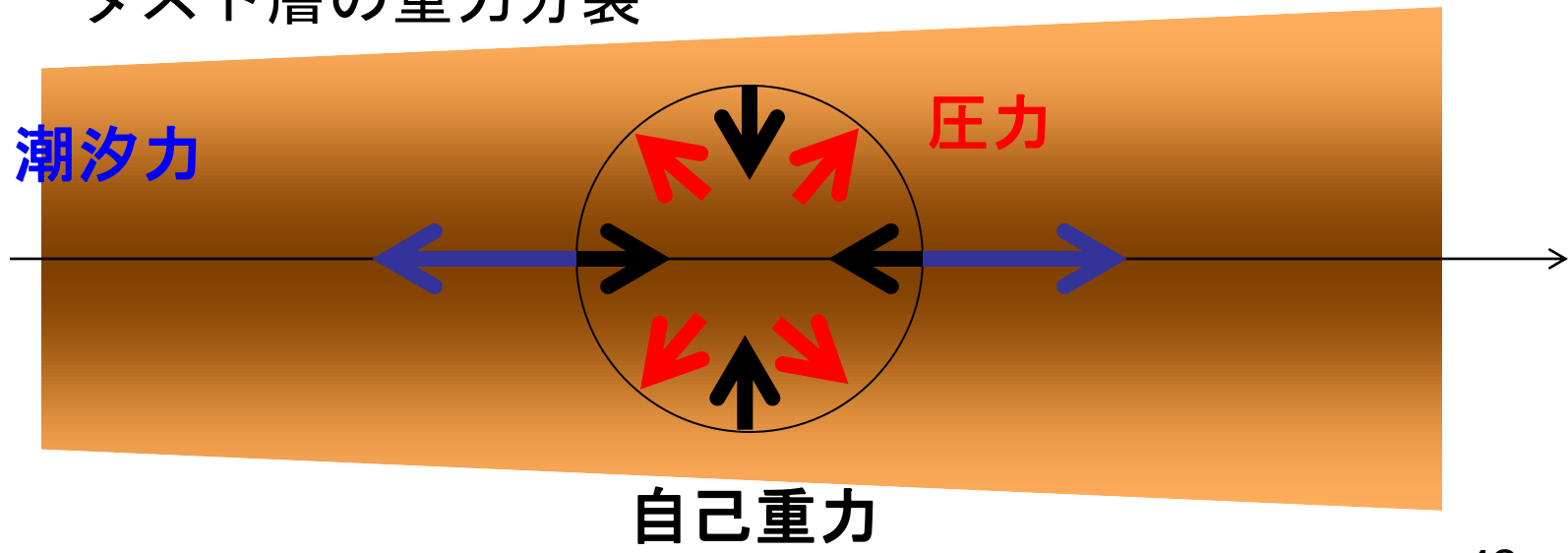

円盤の重力不安定

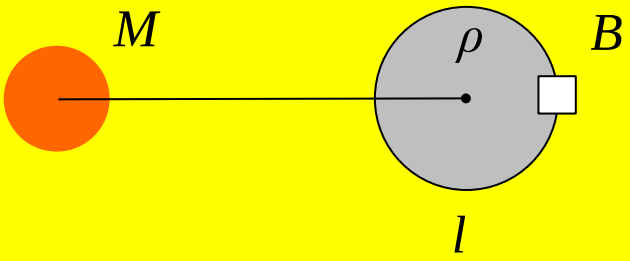

$$a = \frac{c_s^2}{l} - \frac{4\pi G r l^3 / 3}{l^2} + 2\Omega_K^2 l$$

単位質量に働く力(加速度)

↓

$$\frac{a}{l} = \frac{c_s^2}{l^2} - \frac{4\pi G r l / 3}{l} + 2\Omega_K^2$$

l で割る

↓

$$\omega^2 = c_s^2 k^2 - 4\pi G \Sigma k / 3 + 2\Omega_K^2$$

$\Sigma = r l$

$k = \frac{1}{l}$

ちゃんとした線形安定性解析によると,

$$\omega^2 = c_s^2 k^2 - 2\pi G \Sigma k + \Omega_K^2$$

$$\delta r(t) \propto \exp\left[i(kx - \omega t)\right]$$

ロッシュ限界

ρとrを固定，R を変える → r_R が変化する　$r_R = \dfrac{2M}{\frac{4\rho}{3}R^3}$

$$r_H = \left(\frac{m_1}{2M}\right)^{1/3} \quad R = \left(\frac{4\rho/3 \times r\, r^3}{2M}\right)^{1/3} \quad R = \left(\frac{r}{r_R}\right)^{1/3} r$$

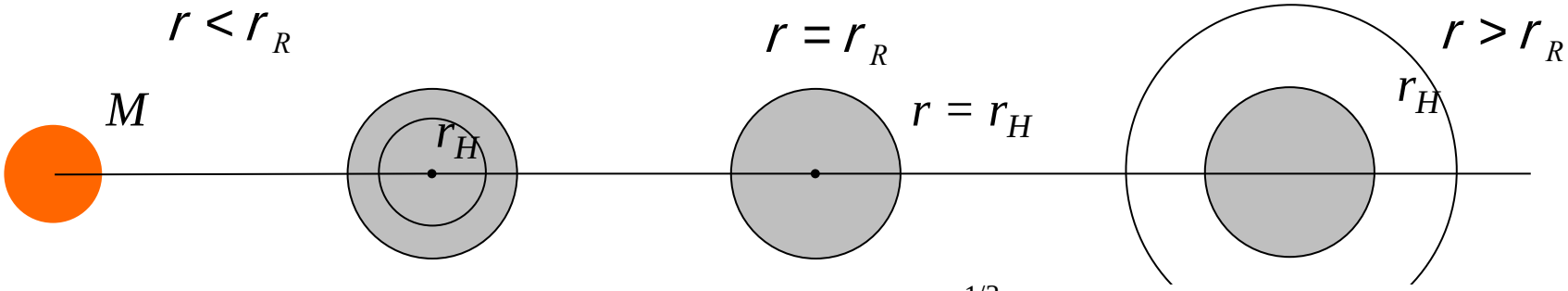

自己重力 < 潮汐力

$$R_R = \left(\frac{2M}{4\rho/3 \times r}\right)^{1/3}$$

自己重力 > 潮汐力

ロッシュ限界

「重力不安定」は起こるか？

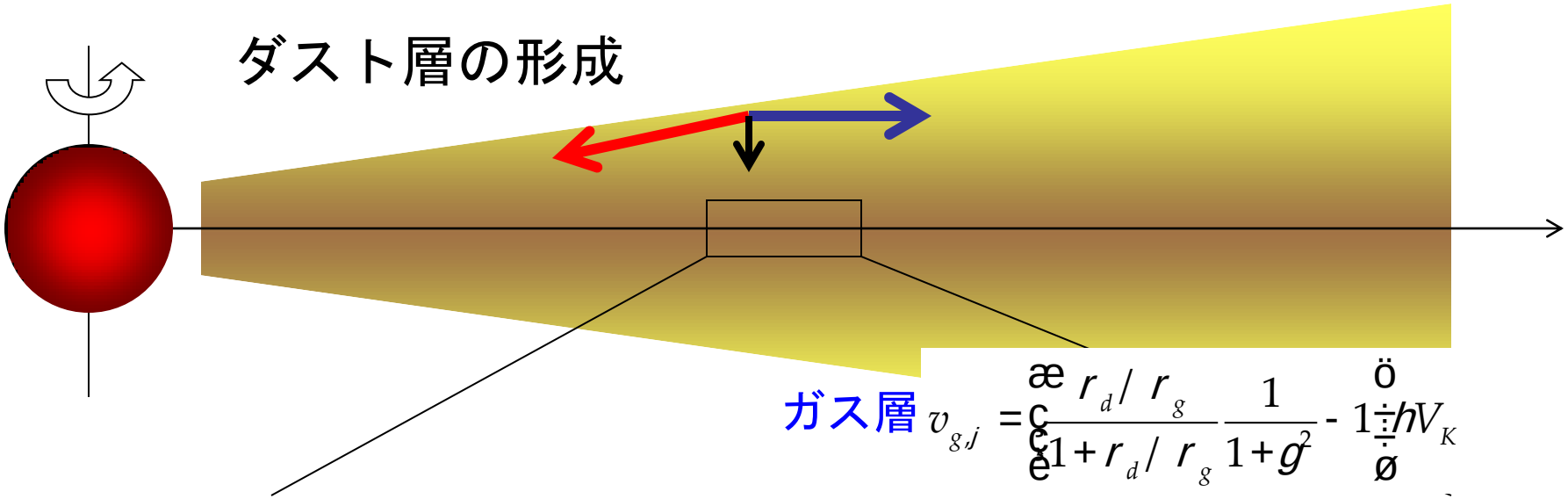
ダスト層の形成
ガス層 $v_{g,j} = \left(\frac{1 + r_d / r_g}{1 + r_d / r_g} \frac{1}{1 + g^2} - 1 \right) hV_K$

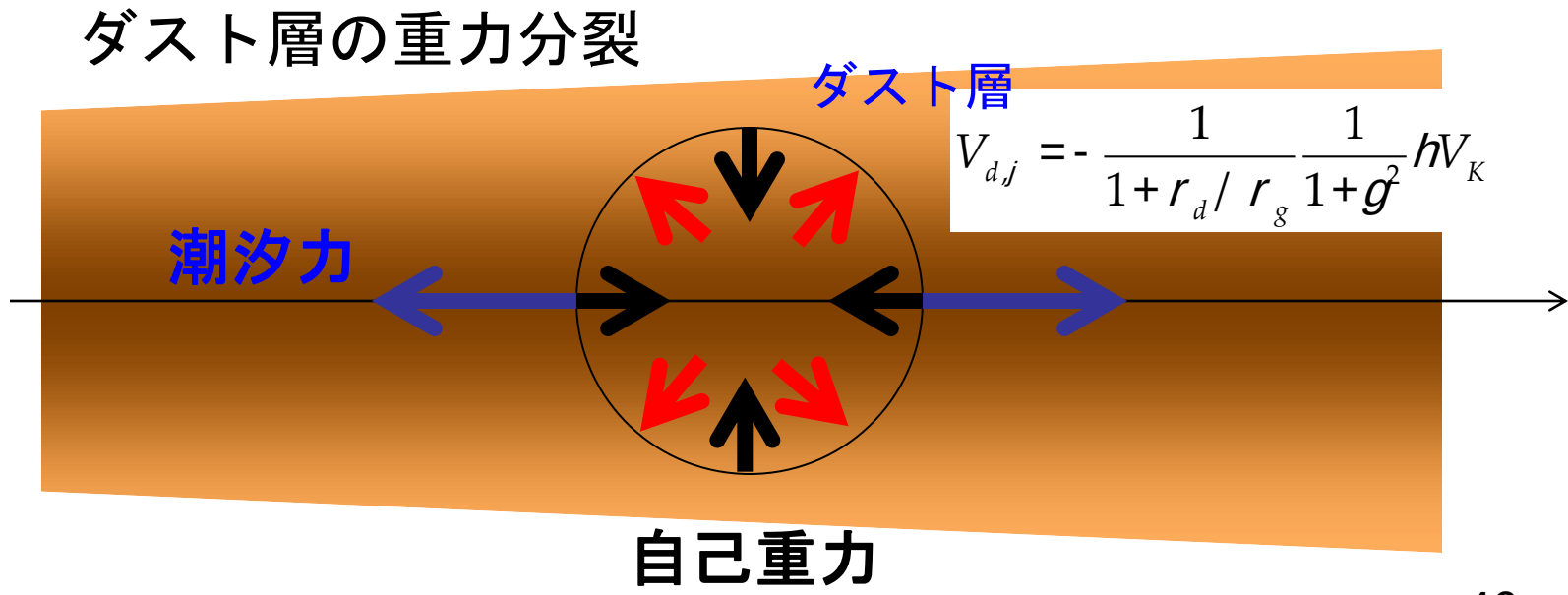
ダスト層の重力分裂
ダスト層
$V_{d,j} = - \frac{1}{1 + r_d / r_g} \frac{1}{1 + g^2} hV_K$
潮汐力
自己重力

Kelvin-Helmholtz不安定

wikipedia

どこかで

$$\mathrm{Ri} = -\frac{g}{r}\frac{dr/dz}{\left(dv_j/dz\right)^2} < \frac{1}{4}$$

のとき，不安定

Sekiya 1998

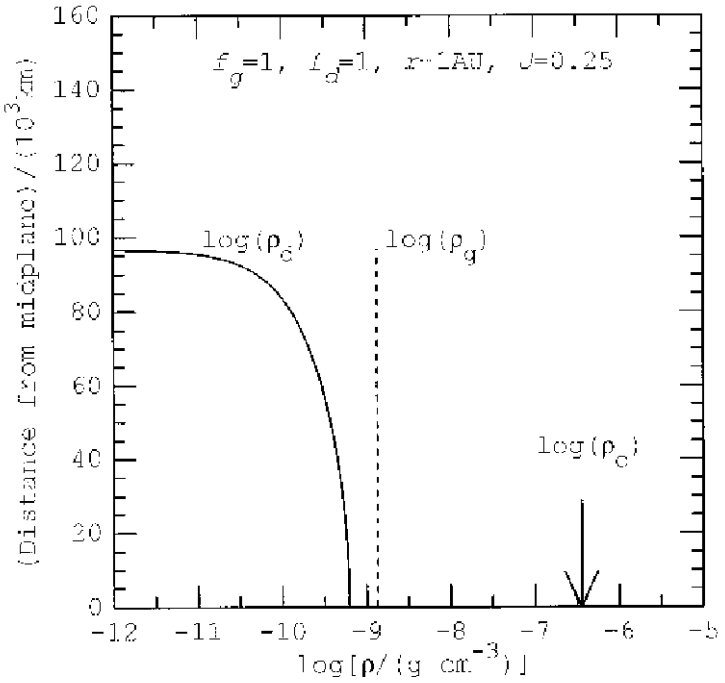

FIG. 1. The critical Richardson number density distribution of dust for model A (solid curve). The gas density distribution is also drawn (dotted line). The arrow shows the critical density of the gravitational stability.

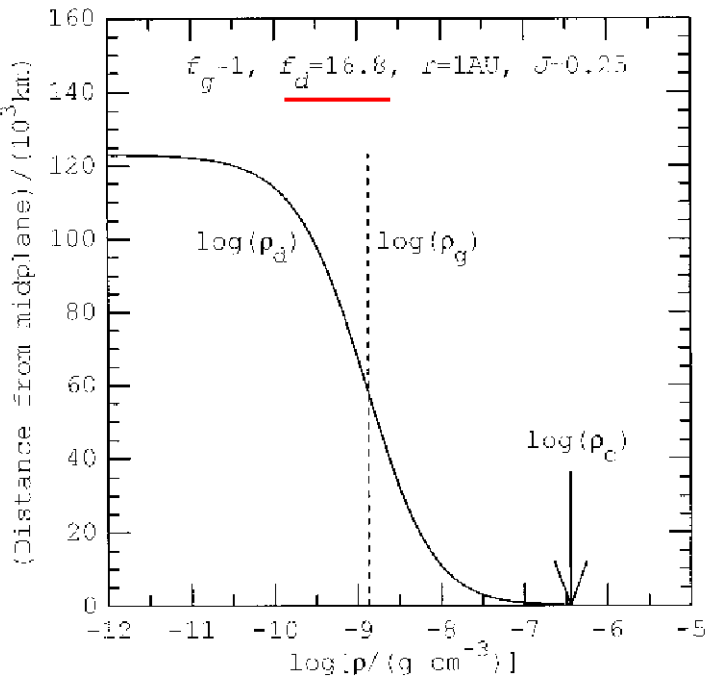

FIG. 2. Same as Fig. 1, but for model B. The dust density distribution has a sharp peak at $z = 0$, where the dust density ρ_d is equal to the critical density ρ_c.

ダストが，MMSNより10倍程度以上濃集すれば，
ダスト層の重力不安定は起こる

乱流中でダスト集積 → 重力不安定

★ Streaming Instability　　Youdin & Goodman 2005

Nakagawa et al. 1986 の定常解は不安定

粒子速度と
方位角方向速度
のゆらぎ

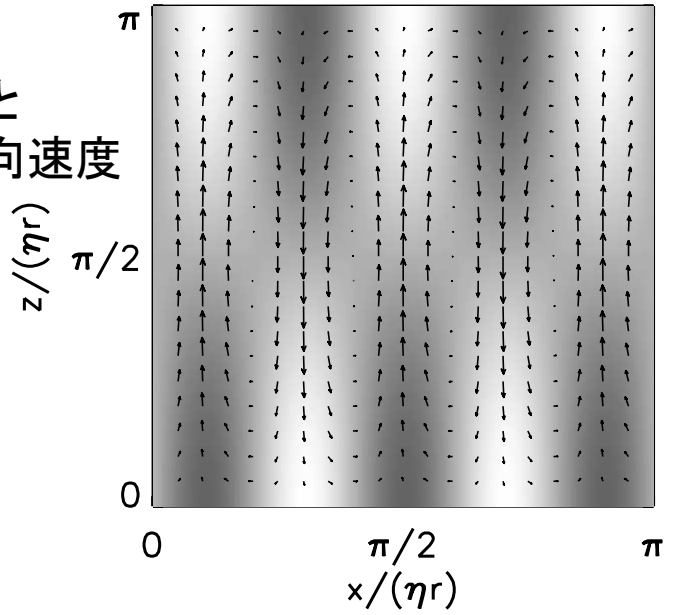

FIG. 5.—Instantaneous (perturbed) particle velocity $\boldsymbol{v}_p$ in the x-z plane with a gray-scale image of azimuthal velocities (white is positive) for a growing mode with $K_x = 5$, $|K_z| = 1$, $\tau_s \approx .044$, and $\rho_p/\rho_g = 0.2$. Gas velocities are very similar because of strong coupling. The density is very nearly in phase with the azimuthal speed, so the vertical flow is channeled to high-density regions. The ratio of azimuthal to vertical velocity amplitudes is $|v_p|/|w_p| \simeq 0.66$. The radial-to-vertical ratio, $|u_p|/|w_p| \simeq K_z/K_x = 0.2$, follows from near incompressibility. This mode has a growth rate $s/\Omega \approx 2.9\times10^{-3}$ and a phase speed $\omega_{\Re}/k_x = -0.42|\Delta U|$.

ガス速度と
密度の
ゆらぎ

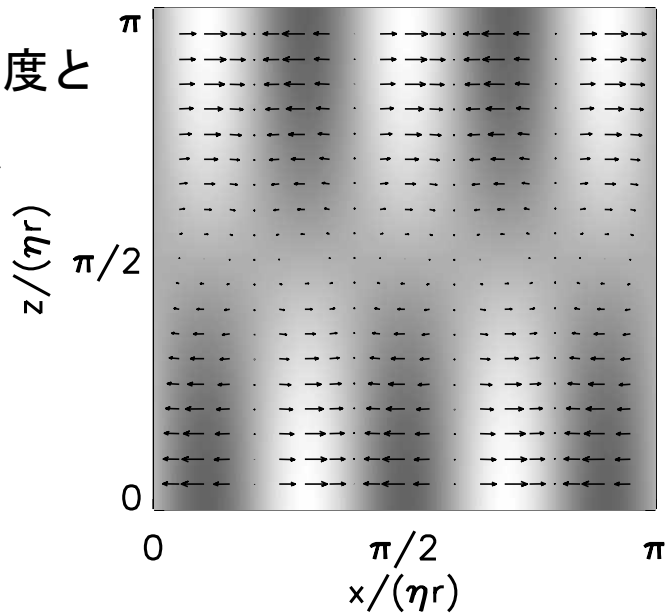

FIG. 6.—Perturbed relative motion of solids and gas, $\Delta\boldsymbol{v}$, for the same mode as Fig. 5. The gray-scale image shows density perturbations (white is positive). The radial relative motion dominates the azimuthal, $|\Delta v|/|\Delta u| \approx 0.15$, and vertical, $|\Delta w|/|\Delta u| \approx 0.11$, speeds. Density perturbations correlate with relative motion.

SI：非線型数値計算

Johansen & Youdin 2007

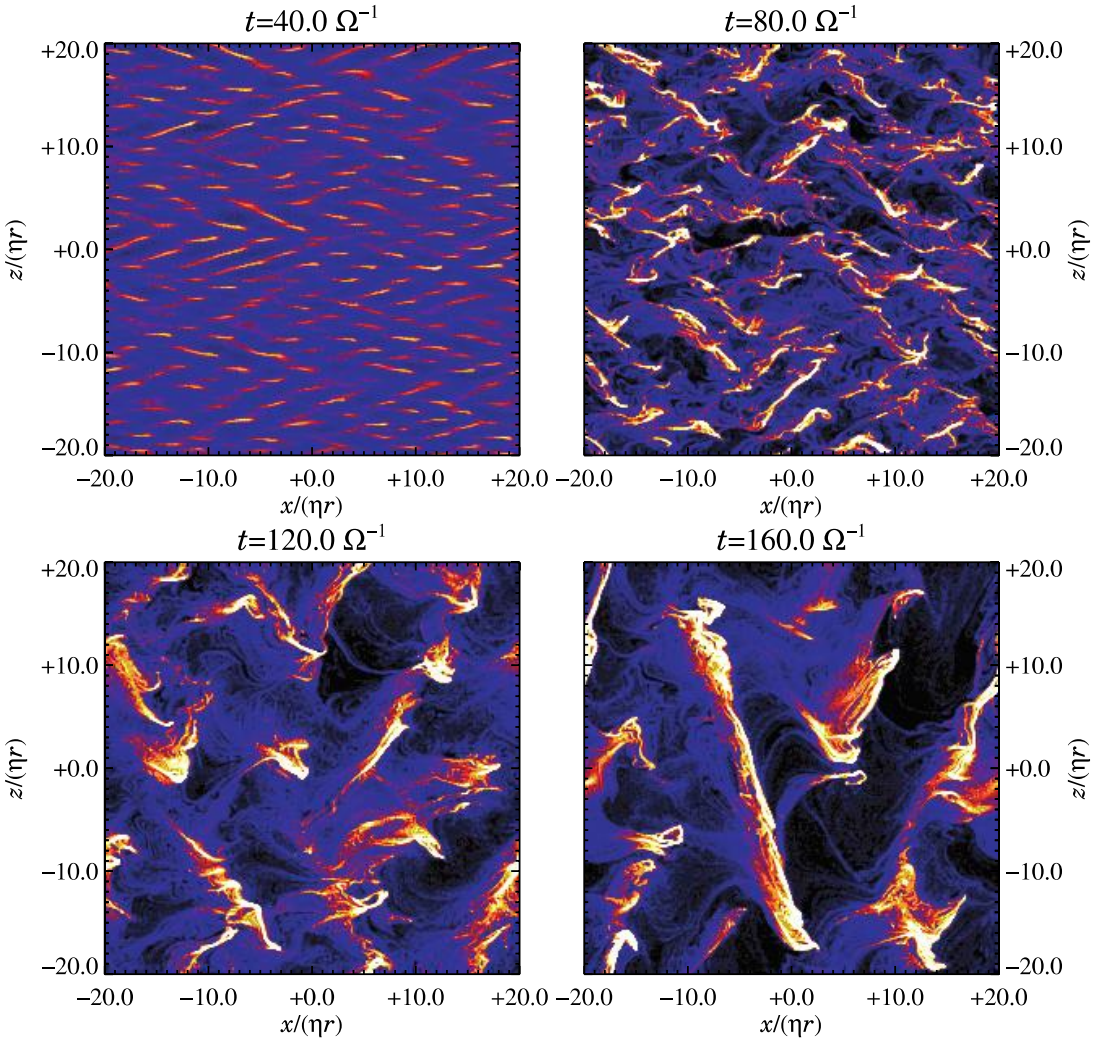

FIG. 2.—Particle density snapshots for run BA with friction time $\tau_s = 1.0$ and a solids-to-gas ratio of $\epsilon = 0.2$. Particle densities increase from black (zero density) to bright yellow/white (solids-to-gas of unity or higher). The evident linear wavelength in the top left panel results from the streaming instability feeding off the drift of the particles through the gas. Subsequent panels document a surprising consequence of the self-consistently generated turbulence: the nonlinear cascade of dense particle clumps into larger filaments. [*This figure is available as an mpeg animation in the electronic edition of the Journal.*]

SI + GI による微惑星形成

Johansen et al. 2007

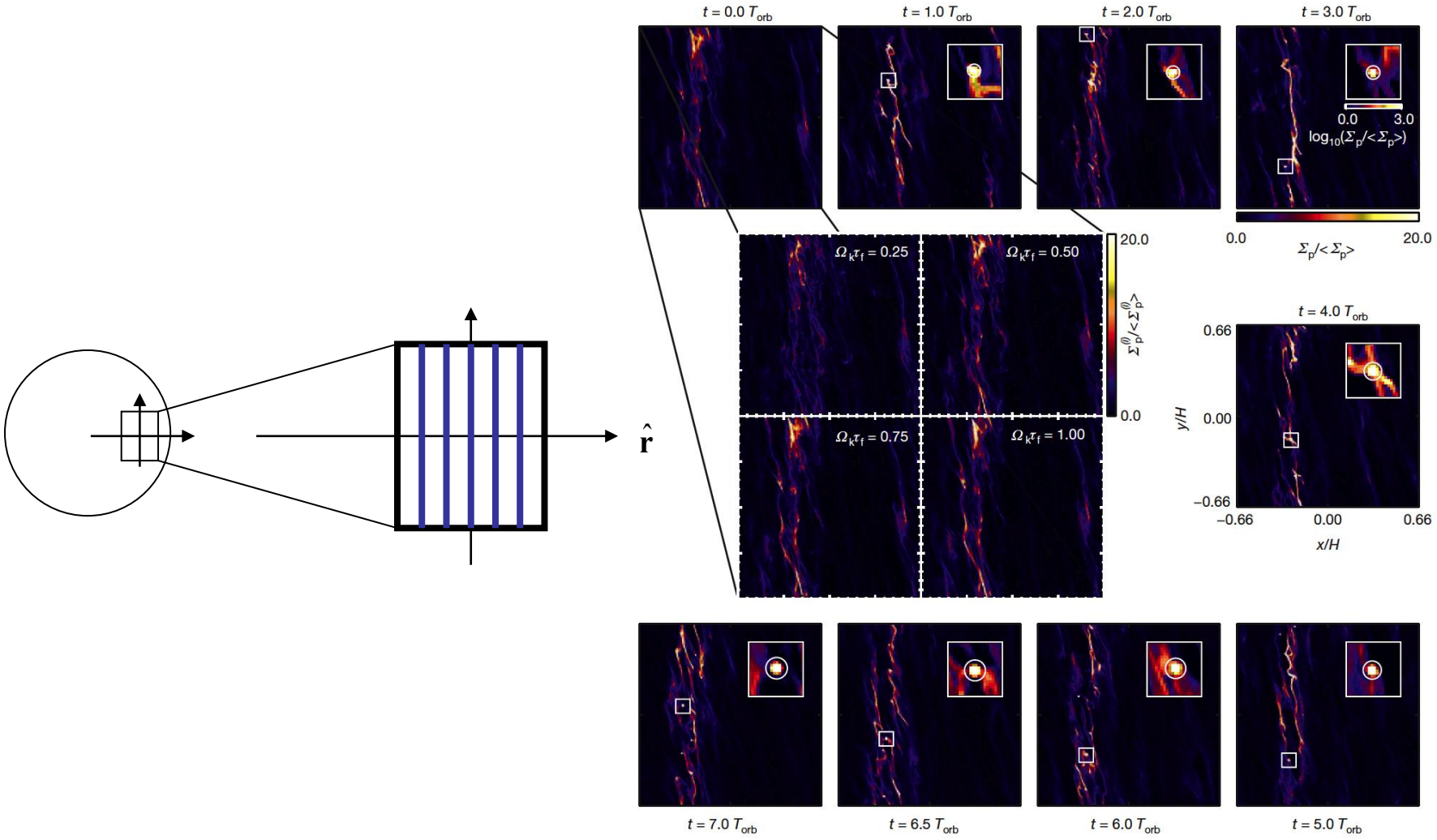

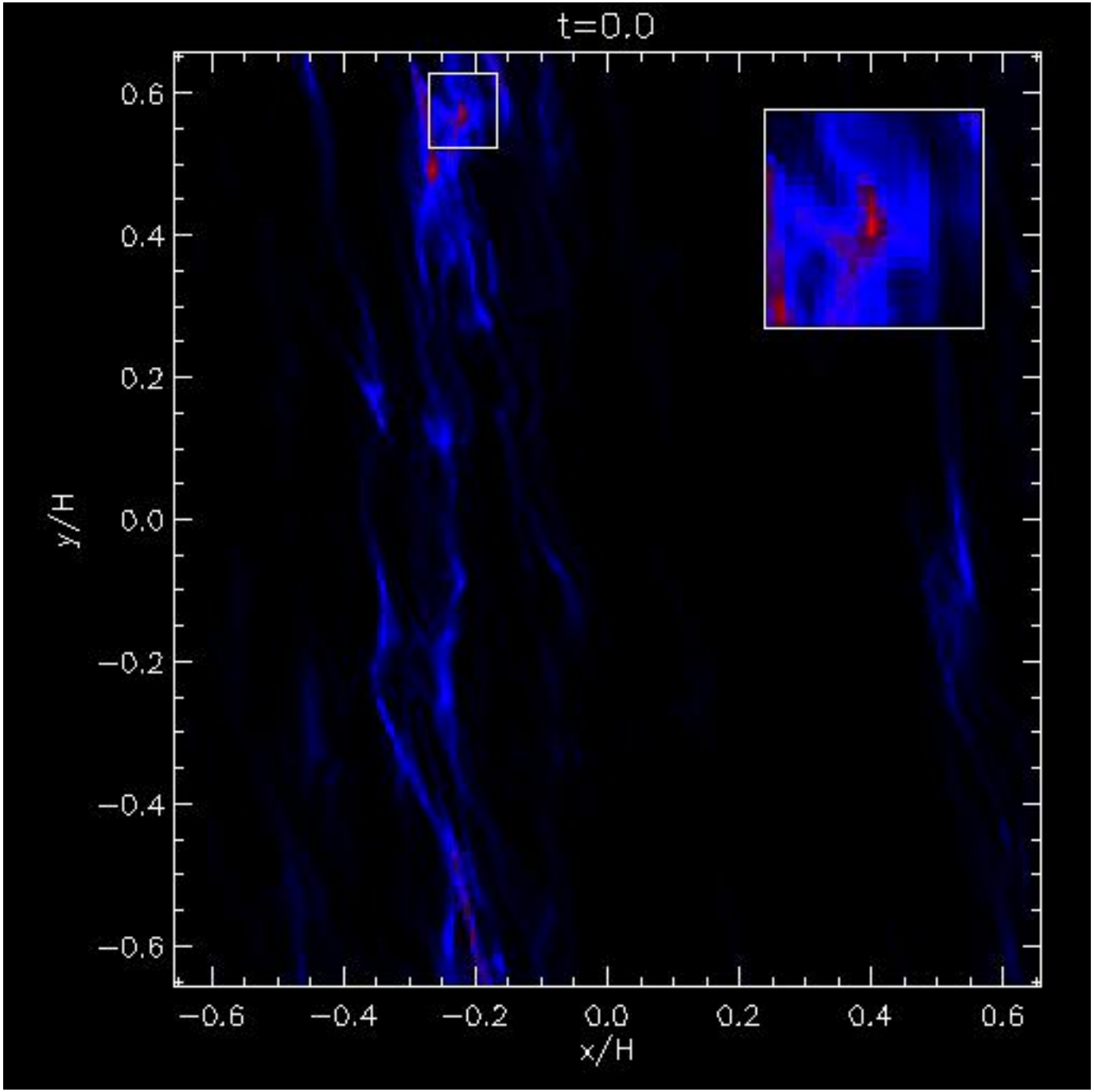

Johansen et al. 2007

~1000km
の微惑星

Bai & Stone 2010

- SI
- ダストのサイズ分布

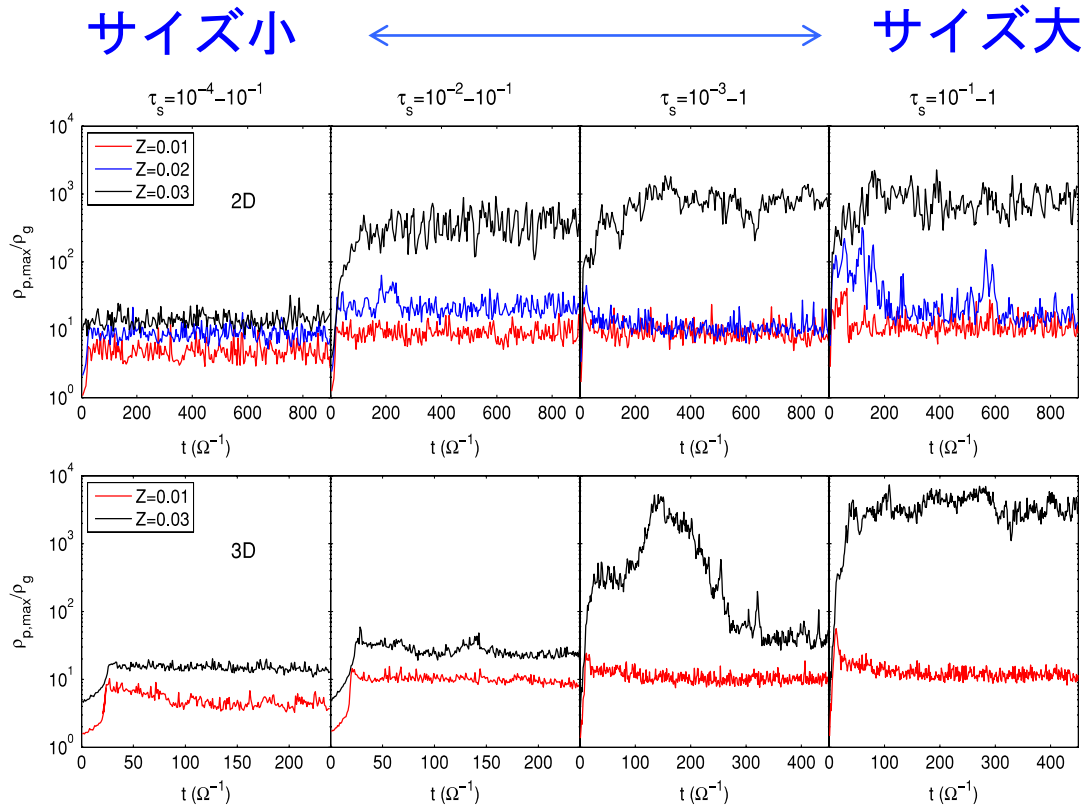

Figure 5. Evolution of maximum particle density for all our simulations. Each panel shows the results from one run series. In the upper panels, red, blue, and black curves label 2D simulations with $Z = 0.01$, 0.02, and 0.03, respectively. The 3D results are shown in the lower panels with $Z = 0.01$ and 0.03 marked with red and black. The maximum density is normalized with respect to the background gas density at the disk midplane.

- 大きなダストがSIに寄与
- サイズが大きいとき，かつ，ダスト濃度が高いとき，大きなダスト濃集が起こる
- *r*方向の移動速度が減る

“Turbulent Concentration”

Cuzzi et al. 2001

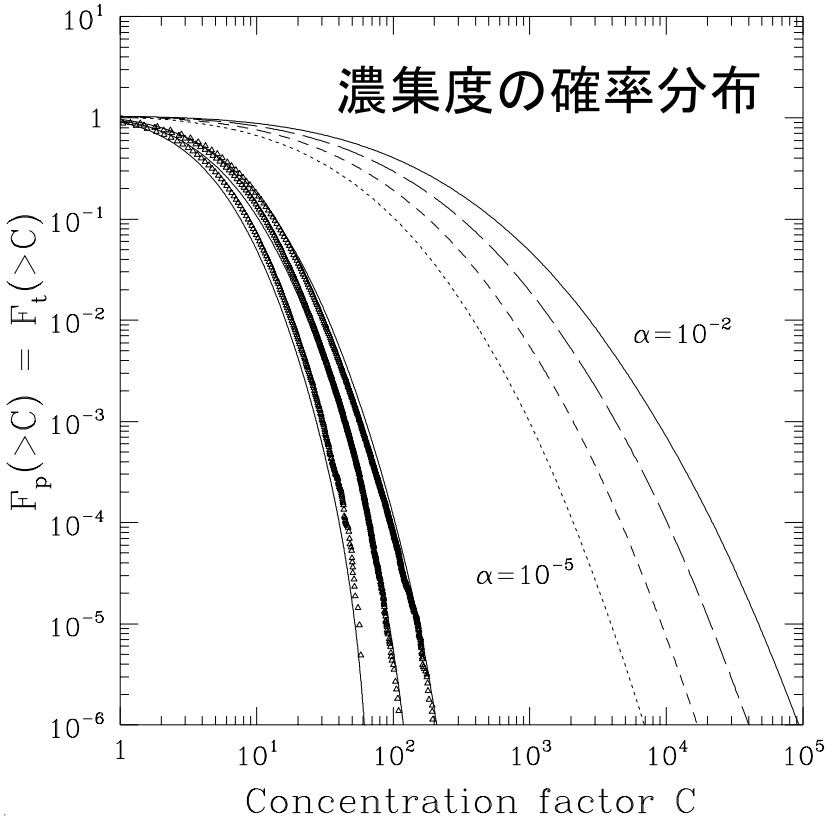

FIG. 4.—Probability distribution functions (PDF's) for the fraction of particles lying in regions with concentration factor greater than C [$F_p(>C)$], or, equivalently, the fraction of time spent by any particle in such regions [$F_t(>C)$]. The three sets of points are binned directly from our numerical simulations; the associated curves are calculated from a single averaged $f(a)$ obtained from all three values of Re (dashed curve in Fig. 3). As discussed in § 5.2, the curves without points use the same $f(a)$ to predict PDF's at the larger Re corresponding to four plausible nebula α values: 10^{-2} (*solid line*), 10^{-3} (*long-dashed line*), 10^{-4} (*short dashed line*), and 10^{-5} (*dotted line*).

“Secular GI”

classical GI + ガス抵抗 → 潮汐力の効果が無力化される

Youdin 2005

- 波長大

ダスト量がMMSNより少し多ければ,
重力不安定が進行 → GIによる微惑星形成

Takeuchi & Ida 2012

まとめ

- ダストの組成変化，移動
- ダストの衝突・成長・破壊
- 微惑星の形成

参考文献

- Abraham et al., Episodic formation of cometary material in the outburst of a young Sun-like star, Nature, 459, pp. 224-226, 2009.
- Bai and Stone, Dynamics of Solids in the Midplane of Protoplanetary Disks: Implications for Planetesimal Formation, The Astrophysical Journal, Volume 722, Issue 2, pp. 1437-1459, 2010.
- Cuzzi et al., Size-selective Concentration of Chondrules and Other Small Particles in Protoplanetary Nebula Turbulence, The Astrophysical Journal, Volume 546, Issue 1, pp. 496-508, 2001.
- Charles et al., Star's Green Crystal 'Rain' May Solve Comet Mystery, NASA press-release, 26 May 2011.
- Davies et al., The Detection of Water Ice in Comet Hale-Bopp, Icarus, Volume 127, Issue 1, pp. 238-245, 1987.
- Goldreich and Ward, The Formation of Planetesimals, Astrophysical Journal, Vol. 183, pp. 1051-1062, 1973.
- Johansen et al., Rapid planetesimal formation in turbulent circumstellar disks, Nature, Volume 448, Issue 7157, pp. 1022-1025, 2007.

参考文献

- Johansen and Youdin, Protoplanetary Disk Turbulence Driven by the Streaming Instability: Nonlinear Saturation and Particle Concentration, The Astrophysical Journal, Volume 662, Issue 1, pp. 627-641, 2007.
- Kawakita et al., Spin Temperatures of Ammonia and Water Molecules in Comets, The Astrophysical Journal, Volume 601, Issue 2, pp. 1152-1158, 2004.
- Kouchi et al., Conditions for condensation and preservation of amorphous ice and crystallinity of astrophysical ices, Astronomy and Astrophysics 290, pp. 1009-1018, 1994.
- Nakagawa et al., Settling and growth of dust particles in a laminar phase of a low-mass solar nebula, Icarus, vol. 67, pp. 375-390, 1986.
- Okuzumi et al., Rapid Coagulation of Porous Dust Aggregates outside the Snow Line: A Pathway to Successful Icy Planetesimal Formation, The Astrophysical Journal, Volume 752, Issue 2, article id. 106, 2012.
- Sargent et al., Dust Processing and Grain Growth in Protoplanetary Disks in the Taurus-Auriga Star-Forming Region, The Astrophysical Journal Supplement, Volume 182, Issue 2, pp. 477-508, 2009.
- Sekiya, Quasi-Equilibrium Density Distributions of Small Dust Aggregations in the Solar Nebula, Icarus, Volume 133, Issue 2, pp. 298-309, 1998.

参考文献

- Takeuchi and Ida, Minimum Dust Abundances for Planetesimal Formation via Secular Gravitational Instabilities, The Astrophysical Journal, Volume 749, Issue 1, article id. 89, 2012.
- van Boekel et al., The building blocks of planets within the 'terrestrial' region of protoplanetary disks, Nature, 432, pp. 479-482, 2004.
- Wada et al., Numerical Simulation of Dust Aggregate Collisions. I. Compression and Disruption of Two-Dimensional Aggregates, The Astrophysical Journal, Volume 661, Issue 1, pp. 320-333, 2007.
- Wada et al., Numerical Simulation of Dust Aggregate Collisions. II. Compression and Disruption of Three-Dimensional Aggregates in Head-on Collisions, The Astrophysical Journal, Volume 677, Issue 2, pp. 1296-1308, 2008.
- Wada et al., Collisional Growth Conditions for Dust Aggregates, The Astrophysical Journal, Volume 702, Issue 2, pp. 1490-1501, 2009.
- Youdin and Goodman, Streaming Instabilities in Protoplanetary Disks, The Astrophysical Journal, Volume 620, Issue 1, pp. 459-469, 2005.
- Youdin, Planetesimal Formation By Dissipative Gravitational Instability, Protostars and Planets V, No. 1286, p.8401, 2005.